A TRIDENT SCHOLAR PROJECT REPORT

NO. 468

Magnetotransport Properties of Shallow Quantum Well Structures for Spintronic Application

by

Midshipman 1/C Benjamin R. Dunphy, USN

UNITED STATES NAVAL ACADEMY
ANNAPOLIS, MARYLAND

USNA-1531-2

REPORT DOCUMENTATION PAGE

Form Approved
OMB No. 0704-0188

1. REPORT DATE *(DD-MM-YYYY)*	**2. REPORT TYPE**	**3. DATES COVERED** *(From - To)*
05-21-18		

4. TITLE AND SUBTITLE
Magnetotransport Properties of Shallow Quantum Well Structures for Spintronic Application

5a. CONTRACT NUMBER

5b. GRANT NUMBER

5c. PROGRAM ELEMENT NUMBER

6. AUTHOR(S)
Dunphy, Benjamin R.

5d. PROJECT NUMBER

5e. TASK NUMBER

5f. WORK UNIT NUMBER

7. PERFORMING ORGANIZATION NAME(S) AND ADDRESS(ES)

8. PERFORMING ORGANIZATION REPORT NUMBER

9. SPONSORING / MONITORING AGENCY NAME(S) AND ADDRESS(ES)
U.S. Naval Academy
Annapolis, MD 21402

10. SPONSOR/MONITOR'S ACRONYM(S)

11. SPONSOR/MONITOR'S REPORT NUMBER(S)
Trident Scholar Report no. 468 (2018)

12. DISTRIBUTION / AVAILABILITY STATEMENT

This document has been approved for public release; its distribution is UNLIMITED.

13. SUPPLEMENTARY NOTES

14. ABSTRACT

Spintronic devices manipulate, generate, and detect spin currents rather than the charge currents found in electronic devices. This requires the materials employed to have large spin-orbit coupling and excellent semiconducting properties. This project focused on n-doped InAlSb/InAs/AlGaSb heterostructures which show promise in spintronic applications. These materials have an InAs quantum well near the surface for easy injection and detection of current and have been optimized to have high electron mobility at room temperature. This project investigated the effect of the well surface proximity on the semiconducting and the spin-orbit properties of these materials to establish their potential for spintronic applications. To this end, we measured and evaluated competing electron transport mechanisms present in these shallow wells and responsible for the observed behaviors.
The sample heterostuctures were fabricated in Hall bars and their sheet and Hall resistance in variable magnetic field, temperature, and illumination conditions, with wavelengths of 400nm up to 1300nm were measured. We then analyzed the Shubnikov-de Haas oscillations and the Hall effect to extract the semiconducting and spin-orbit properties of these structures. The results are compared and contrasted with the properties of a deep-channel InAs sample with excellent spinorbit coupling properties. We find that the carrier concentration of the shallow channels increases under infrared illumination, but decreases when further decreasing the wavelength. We also find a general increase in the effective mass of the samples with the carrier concentration. Lastly, we find that the shallow-well samples do not exhibit observable spin orbit coupling despite excellent semiconducting properties. We conclude that small quantum scattering times make resolving the spin-split populations difficult.

15. SUBJECT TERMS
Magnetotransport, Heterostructures, Spintronics, Shubnikov-de Haas oscillations, InAs

16. SECURITY CLASSIFICATION OF:			**17. LIMITATION OF ABSTRACT**	**18. NUMBER OF PAGES**	**19a. NAME OF RESPONSIBLE PERSON**
a. REPORT	**b. ABSTRACT**	**c. THIS PAGE**		48	**19b. TELEPHONE NUMBER** *(include area code)*

U.S.N.A. --- Trident Scholar project report; no. 468 (2018)

MAGNETOTRANSPORT PROPERTIES OF SHALLOW QUANTUM WELL STRUCTURES FOR SPINTRONIC APPLICATION

by

Midshipman 1/C Benjamin R. Dunphy
United States Naval Academy
Annapolis, Maryland

_____
(signature)

Certification of Adviser(s) Approval

Associate Professor Elena Cimpoiasu
Physics Department

_____
(signature)

_____
(date)

Dr. Brian R. Bennett
Office of Naval Research

_____
(signature)

_____
(date)

Acceptance for the Trident Scholar Committee

Professor Maria J. Schroeder
Associate Director of Midshipman Research

_____
(signature)

_____
(date)

Abstract

The electron is a fundamental particle that carries both an electric charge and an intrinsic angular momentum (spin). Recently, interest in employing the electron's spin triggered a wave of research in spin-dependent electron transport in various materials (spintronics). Spintronic devices manipulate, generate, and detect spin currents rather than the charge currents found in electronic devices. This requires the materials employed to have large spin-orbit coupling and excellent semiconducting properties.

This project focused on n-doped InAlSb/InAs/AlGaSb heterostructures which show promise in spintronic applications. These materials have an InAs quantum well near the surface for easy injection and detection of current and have been optimized to have high electron mobility at room temperature. This project investigated the effect of the well surface proximity on the semiconducting and the spin-orbit properties of these materials to establish their potential for spintronic applications. To this end, we measured and evaluated competing electron transport mechanisms present in these shallow wells and responsible for the observed behaviors.

The sample heterostuctures were fabricated in Hall bars and their sheet and Hall resistance in variable magnetic field, temperature, and illumination conditions, with wavelengths of 400nm up to 1300nm were measured. We then analyzed the Shubnikov-de Haas oscillations and the Hall effect to extract the semiconducting and spin-orbit properties of these structures. The results are compared and contrasted with the properties of a deep-channel InAs sample with excellent spin-orbit coupling properties. We find that the carrier concentration of the shallow channels increases under infrared illumination, but decreases when further decreasing the wavelength. We also find a general increase in the effective mass of the samples with the carrier concentration. Lastly, we find that the shallow-well samples do not exhibit observable spin orbit coupling despite excellent semiconducting properties. We conclude that small quantum scattering times make resolving the spin-split populations difficult.

Keywords: Magnetotransport, Heterostructures, Spintronics, Shubnikov-de Haas oscillations, InAs

Acknowledgments

I would like the thank the Materials Science and Technology Division at the Naval Research Laboratory for growing and fabricating the samples used in this project. Specifically, I would like to thank Joseph Christodoulides and Shawn Mack for agreeing to collaborate on this project. I would also like to thank Dr. Brian Bennett from the Office of Naval Research for providing not only the samples themselves but also for his guidance and advice. Finally, I would like to thank my chief advisor, Professor Elena Cimpoiasu, for her constant instruction and patience throughout this project.

Contents

1 Introduction

Modern technological advancements are built upon computers and data processing units with sophisticated circuitry. These technologies transmit information using electrical currents, that is, the manipulation of charge. However, electrons exhibit another degree of freedom, namely spin, which can be employed in a similar fashion. The emerging field of spintronics focuses on electronic applications in which the spin degree of freedom is used. The ultimate goal of this field is spin-based technologies that generate, manipulate, and detect spin currents, analogous to charge currents in electronics. Evidence of the importance of this spin-based technology is the giant magnetoresistive effect which was at the heart of commercial applications like magnetic read heads for ultragigabyte storage disk drives and magnetic RAMs [1]. Albert Fert and Peter Grunberg, who discovered the giant magnetoresistive effect in ferromagnet/metal/ferromagnet structures, received the Nobel prize in 2007 for their discovery. Furthermore, additional spintronic applications include MRAM, computer memory that combines traditional RAM and hard drive, and chips that combine logic and memory devices. These applications could potentially revolutionize the design of computers and other electronic devices.

(a) **Field Effect Transistor**

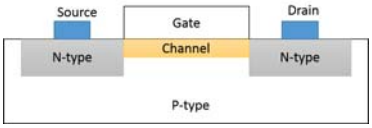

(b) **Spin Field Effect Transistor**

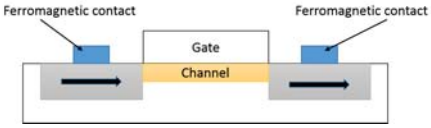

Figure 1: *Above are side-by-side comparisons of the traditional field-effect transistor and the spin field-effect transistor. In the spin FET, the gate modulates the current flow through spin-orbit coupling.*

A promising technological application of spin physics is the spin field-effect transistor (FET). The spin FET was first proposed by Datta and Das [2] and first demonstrated successfully by a collaboration between the the Naval Research Laboratory and the Korean Institute of Science and Technology in 2009 [3]. The spin FET is based on the design of a traditional field-effect transistor (see Figure 1). The traditional FET has three main contacts: source, drain, and gate. Electric current flows between the source and the drain contacts through the channel. Upon the application of a gate voltage, the current between the source and drain can either be turned on or off, like water through a faucet. This forms the foundation of the binary language, commonly known as 1's and 0's, which is essential to computer language. Thus, the traditional FET works through manipulation of the flow of charge. The spin FET works in a similar fashion but it generates, detects and manipulates the *spin polarization* of the currents rather than charge current itself. The spin-

FET assumes ferromagnetic source and drain contacts with parallel magnetizations. The intensity of the source-drain current depends on the spin orientation of the carriers moving between the two electrodes with regard to the spin-orientation in the source and drain contacts. This orientation can be modulated through the application of a gate voltage via spin-orbit coupling. Spin-orbit coupling is a relativistic effect where the spin magnetic moment of the electron acts as a mini bar magnet and couples with relativistic-magnetic fields that are transverse to the electron's trajectory. In solids, this effect can be either intrinsic or extrinsic and may be enhanced by the addition of a gate electrode [4]. Through this method, a spin FET can generate, manipulate, and detect spin currents without the need of an externally applied magnetic field.

Our project focused on the interplay between spin-orbit coupling, electron transport properties, material design, and photoconductivity on the feasibility of a spin FET design. Since the spin FET relies heavily on the physics of **spin-orbit coupling**, a detailed understanding of the phenomena and technoligical limitations of spin-orbit coupling is absolutely necessary. From a practical perspective, materials used for a spin FET need high mobility and large carrier concentrations, strong spin-orbit coupling properties, and shallow channels for optimized spin injections. These properties can be designed for and optimized in a material called a heterostructure. A heterostructure is a material whose composition changes as a function of position, generally its position relative to the surface. These materials can be built with high precision by careful deposition of atomic layers of different materials using a technique called molecular beam epitaxy. While there have been reports in literature about heterostructures with large spin-orbit coupling, there is little to no systematic work on heterostructures with shallow channels, which are located close to the surface of the heterostructure. Therefore, this project focused on studying the properties of the various heterostructure samples.

More specifically, this project focused on the relationships between the spin-orbit coupling strength and the basic semiconducting properties of shallow *n*- doped channels in InAlSb/ InAs/AlGaSb heterostructures produced and provided by the Naval Reasearch Laboratory. These samples are unique in that the channels are very shallow, within 7 to 10nm of the surface. This placement optimizes the injection and detection of the spin currents. Additionally, these samples were designed to have high electron mobility at room temperature, making them a promising material for spintronic applications. The samples' electronic properties were measured at USNA using a platform that can produce magnetic fields as high as 9 T and temperatures as low as 1.9 K. Thus, this platform enabled us to study the samples under variable magnetic fields, variable temperatures, and variable orientations with respect to the direction of the magnetic field. With these measurements, we extracted key semiconducting parameters together with the strength of the spin-orbit coupling.

Using these measurements to create a complete picture of the materials' properties, we compared the effect of the positioning of the channel with respect to the surface and the effect of dopant location relative to the channel. We then compared the results with the properties of a deep-channel heterostructure that was commercially developed and shown to have excellent spin-orbit coupling and semiconducting properties. Further, the samples were exposed to different wavelengths of light to examine how the application of light effects the carrier concentration and modulates the spin-orbit coupling. Ultimately, our results provide information about the optimal electric properties of materials for spin-based application, and in particular, describe the feasibility of using these shallow channels for spintronic applications.

2 Background

2.1 Spin-Orbit Coupling

An electron is characterized by two main quantum properties: electric charge and spin [5]. While most of the familiar electromagnetic phenomena are a result of the electric charge, the spin has several physics-profound consequences as well. The most important consequence to spintronics is the phenomenon of spin-orbit coupling [6–8]. In a hydrogen atom, spin-orbit coupling is a relativistic effect where the electron in its rest frame sees the proton rotating around it. As a result, the electric field produced by the nucleus is seen as a magnetic field by the electron. The spin magnetic moment of the electron aligns with the magnetic field, thus adding a contribution to the energy of the electron. In solids, spin-orbit coupling works very similarly. In this case, the effective magnetic field seen by the moving electron's spin is a result of electric field asymmetries/variations in the crystalline lattice. The spin magnetic moment of the electron aligns with this magnetic field and produces a contribution to the energy of the electron in the crystal. A uniquely quantum effect, spin-orbit coupling provides a challenge to measure. Two approaches can generally be used. A sophisticated device can be engineered to measure the spin splitting directly, or it can be observed indirectly through **Shubnikov-de Haas oscillations**. We have used the latter approach.

Although a modified version of a spin-based FET has been successfully demonstrated, many questions with regard to the spin-physics and practical implementation remain. The first and most important controversy relates to the nature and the strength of the spin-orbit coupling as the main tool to manipulate the spin orientations. Additionally, another problem is how to ensure efficient injection and detection of spin currents by the electrodes into the channel.

This project aimed to address these issues by studying shallow n-type channels in III-V heterostructures provided by the Naval Research Laboratory. Systematic analysis of the results will

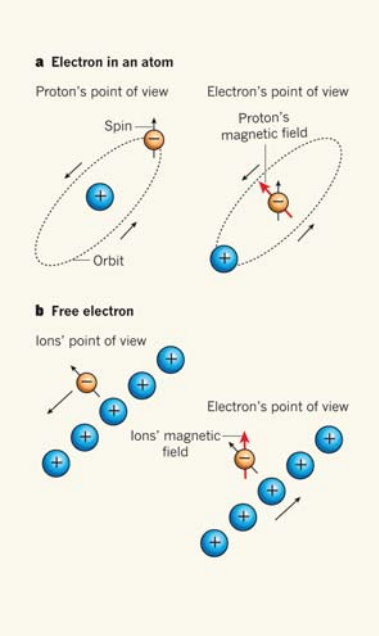

Figure 2: *Diagram of basic Spin-Orbit Coupling for a simple atom and a simplified lattice. Adapted from [9].*

provide valuable data to researchers in the field for construction of future materials for spintronic applications. We next discuss our choice to focus on heterostructures as the candidate materials for spintronic applications.

2.2 Heterostructures

We first consider what the desirable properties of materials suitable for spin-based applications are. From a theoretical perspective, a large energy contribution from spin-orbit coupling is needed to manipulate spin polarizations. To achieve large energy contributions, two things are necessary: a large in-the-crystal effective magnetic field and a large magnetic moment of the electron. The effective magnetic field is due to the motion of the electrons through the transverse magnetic field and is given via $\vec{B} \approx \vec{v} \times \vec{E}$ (See Appendix A). To obtain a large electron velocity, the material needs to have a large mobility. Mobility is a measure of how easily an electron moves through the material. Additionally, there needs to be a large intrinsic transverse electric field which relates directly to the nature of the crystalline lattice. The size of the electron magnetic moment is also important. Since the magnetic moment μ is proportional to the g-factor, a large g-factor is desired. Lastly, there needs to be a strong signal. This requires a lot of carriers to tunnel through the potential barriers to reach the electrodes. To do this, there needs to be a large carrier concentration and shallow wells to provide a smaller barrier to electron tunnelling. Without these last two parameters,

spin-split signals may be created but never read by the device.

The materials chosen for our project samples are heterostructures because they are versatile materials that can be engineered to satisfy the above practical requirements. Grown via molecular beam epitaxy, our samples have precise dimensions and pure layers. Heterostructures can be engineered to create a channel with a large population of electrons that move with high mobility. High concentrations and high mobility are hallmarks of electron gas systems (collections of electrons that, within certain approximations, behave like the molecules in a gas, but obey Fermi-Dirac statistics). Two-dimensional electron gas systems (2DEG) exist in ”quantum wells”, which can be engineered into the heterostructure. They have long been considered an ideal candidate for high speed electron devices because of their large mobility [10] [11].

In Figure 3, a stack of materials that form a heterostructure similar to the ones studied in this project is shown. The channel (i.e. the quantum well) here is the 15 nm InAs. The picture to the right shows the energy band diagram as a function of position, with zero corresponding to the top surface. The Fermi level is indicated by the dashed line. The full lines indicate the bottom of the conduction band (upper) and the top of the valence band (lower). Sharp changes in those lines indicate strong internal electric fields. Since the layer stacking is engineered, these internal electric fields can be enhanced. This is essential to heightening the spin-orbit coupling strength in the material. The “quantum well” is the layer where the two-dimensional electron gas lives. It is indicated with a red circle.

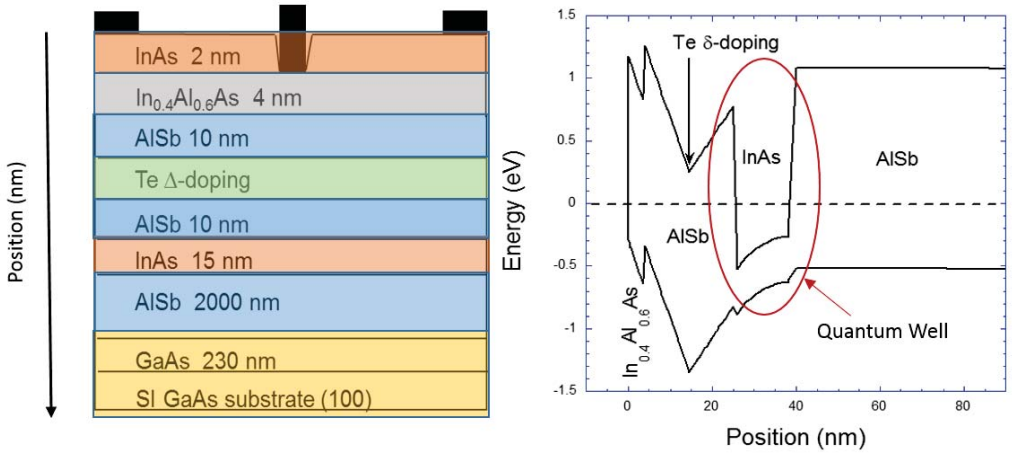

Figure 3: *A diagram of a heterostructure stack with its corresponding energy band diagram. Note that the position axis starts at the top of the stack and works down. Emphasis added. [12]*

2.3 Basic Semiconducting Properties

All semiconducting properties result from the discrete allowed energies of the electron in the semiconductor [13]. The periodic nature of crystalline structure means that the electric potential is periodic in space. This periodic potential structure results in electron states with bands of allowed energies. Within each band, there is a continuum of allowed energies. For our consideration, there are only two bands worth mentioning, the valence band and conduction band. The valence band is the band of energy levels which contains the highest occupied level of bound electrons in the atom. The conduction band is the band of energy where the electrons have enough energy so that they are free to move within the structure. When the valence band and the conduction band overlap, the material is known as a metal because the valence electrons are free to move through the lattice and thus conduct. When there is a large gap between the valence and conduction band, the material is known as an insulator. The electrons are not free to move in the lattice and thus do not conduct.

Semiconductors are insulators with a small energy gap between the valence and conduction bands. As a result, the presence of light or small temperature changes can cause the electrons in the valence band to gain enough energy to ”jump” the gap into the conduction band. These electrons then contribute to the carrier concentration. Furthermore, the holes left behind act as pseudo-positive charges and contribute to the carrier concentration although their mobility is much less. The resistance of a material is directly related to the number of unbounded charges free to move in the material. The number of **free carriers** per unit volume is a quantity known as the carrier concentration. This quantity is signified by n for electrons and p for holes. A high carrier concentration is often desired so impurities, known as dopants, are introduced into the lattice. Dopants work by introducing atoms into the lattice with a slightly different number of valence electrons. This causes either a free electron or a hole to appear in the lattice. Dopants come in two types: n-type increase the number of free electrons and p-type increase the number of holes in the electrons.

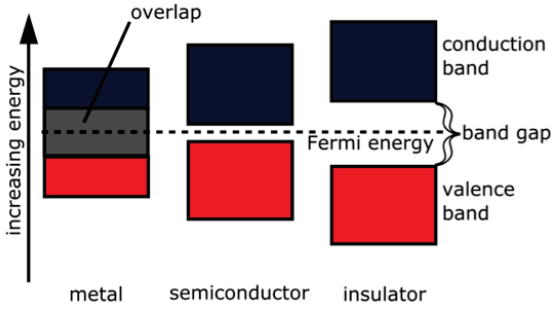

Figure 4: *A comparison of the energy band diagrams of metals, semiconductors, and insulators [14]*

Another important semiconducting property is the **carrier mobility** μ. Carrier mobility relates how much the velocity of the particle is affected by the application of an electric field. The mobility is related to the effective mass of the particle as well as the average time between collisions in the crystal. In short, mobility is a measure of how easily carriers move through the material.

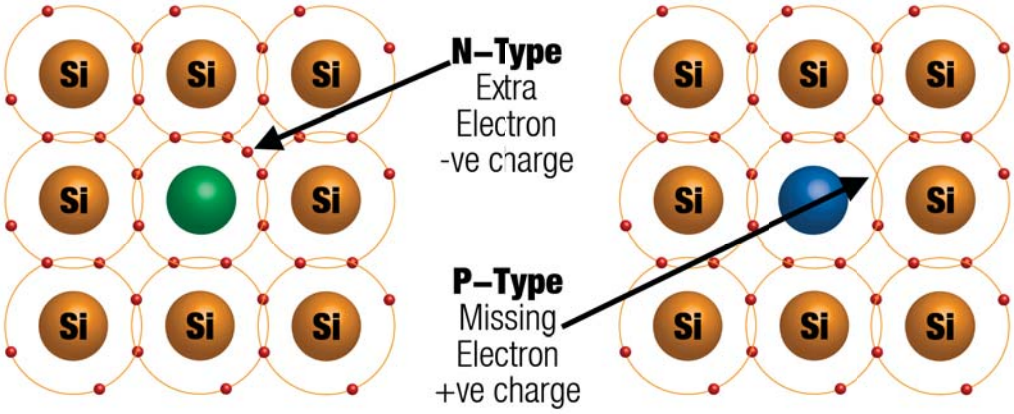

Figure 5: *A cartoon depiction of a Silicon crystalline lattice with n-type (e.g. nitrogen) and p-type (e.g. boron) atoms. [15]*

The charge concentration and mobility can be determined from resistance measurements in low magnetic fields. These measurements find values for longitudinal resistivity ρ_{xx} and the transverse resistivity ρ_{xy} which are related to *n* and μ via:

$$\rho_{xx} = \frac{1}{ne\mu}, \rho_{xy} = \frac{B}{ne} \tag{1}$$

Thus, under these conditions the longitudinal resistivity is a constant of the magnetic field while the transverse resistivity is linearly related.

2.4 The Shubnikov-de Haas oscillations and the Hall Effect

In the presence of a magnetic field, the electrons interact with the magnetic field to produce a force, termed the Lorentz force. The Lorentz force causes the electrons to move in circular orbits. The circular nature of the orbits causes the electrons to interfere with themselves and quantizes the orbits. These quantized orbits are called Landau levels and they have discrete values of energy associated with them given by:

$$E_n = \hbar\omega_c(n + \frac{1}{2}), \tag{2}$$

where $\omega_c = eB/m^*$ is the cyclotron frequency and n is an integer. As a result of the Landau levels, the longitudinal (R_x) and transverse resistance (R_H or R_{xy}) exhibit a strange dependence on the field B at low temperature and high magnetic field (see Figure 6 right). The longitudinal resistance oscillates with B at intermediate field values, reaching a maximum when the Fermi level passes through a Landau level, and minima between the Landau levels. These oscillations are called **Shubnikov-de Haas** oscillations (SdH). The transverse resistance shows a staircase dependence,

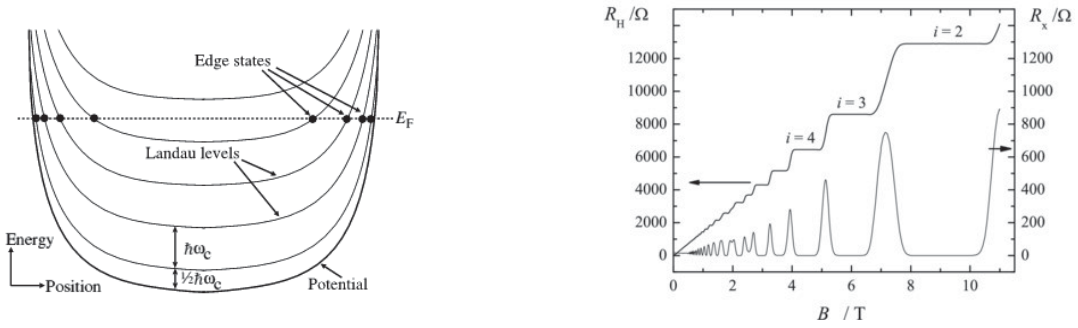

Figure 6: *Landau levels (left) and the resulting integer quantum Hall effect/Shubnikov-de Haas oscillations (right). Adapted from [16]*

with plateaus when the Fermi level passes between the Landau levels. This effect is called the **integer quantum Hall effect**.

The oscillations of the longitudinal resistivity were modeled for the case of a single band conduction in low and intermediate fields with the **amplitude** of the oscillations given by [17]

$$\Delta\rho_{xx}(B)/\rho_{xx}(0) = e^{(-\pi/\omega_c\tau_q)}\frac{2\pi^2 k_B T m^*/\hbar eB}{\sinh \pi^2 k_B T m^*/\hbar eB} \tag{3}$$

From the equation above, it is apparent that the amplitude of the oscillations for a given B is dependent only on the temperature T, the effective mass m^*, and the quantum scattering time τ_q, which relates to the broadening of the Landau levels. By fitting the SdH oscillations to a curve for each value of T, this provides a means to calculate the effective mass and scattering times. Furthermore, the SdH oscillations are periodic in $1/B$ and related to the carrier concentration (see Section 5.1). Thus, analyzing the frequency of the SdH oscillations is an alternative experimental means to determine the carrier concentration.

2.5 Spin-Orbit Coupling and Shubnikov-de Haas Oscillations

The Landau levels seen above are spin degenerate meaning that the particles of different spin have the same energy value. This reflects a simplified view of Landau levels and atomic interactions. In reality, the presence of the spin lifts the degeneracy of the Landau levels in the presence of a magnetic field. Namely, electrons from the same Landau level but with different spin orientations (up or down relative to the magnetic field) occupy different energy levels.

The spin-split Landau levels are most observable in strong applied magnetic fields. This spin splitting is termed the Zeeman effect. However, even in the absence of a strong applied field, the Landau levels are split because of the the spin-orbit coupling. This splitting is observable

in the Shubnikov-de Haas oscillations. As mentioned above, Shubnikov-de Haas oscillations are oscillations in the longitudinal resistance as a function of the magnetic field. The frequency of the oscillations is related to the carrier concentration. However, in the presence of the the spin-orbit coupling, the carrier population is split according to spin orientation, that is parallel or anti-parallel to the effective magnetic field. Since there are now two populations of carriers, there are two frequencies of oscillations. In the same way that two similar sound frequencies cause a beat to form, these two frequencies cause a beat to form in the Shubnikov-de Haas oscillations. Since

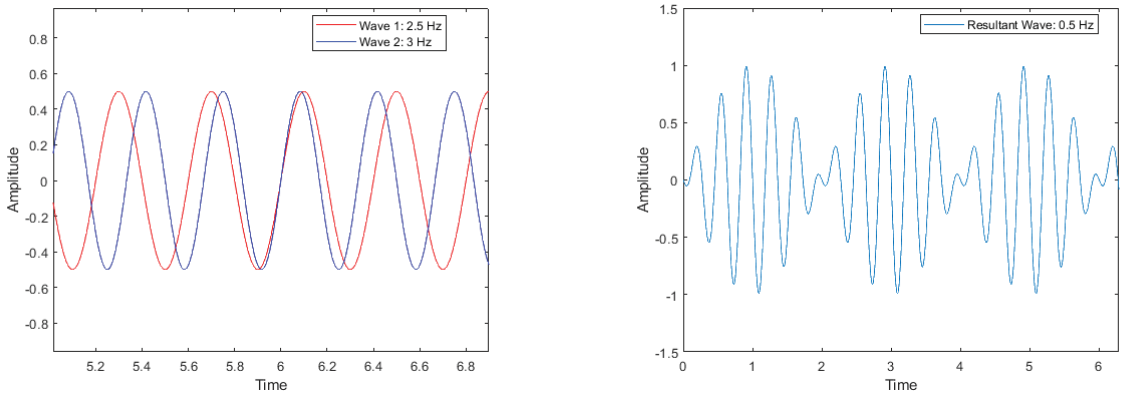

Figure 7: *Example of the formation of beats. The graph on the left shows two waves with their respective frequencies. The graph on the right shows the resultant wave with a frequency equal to the difference in frequencies of the input waves. A similar process occurs for the SdH oscillations.*

the frequency of the beat is related via $f_{beat} = f_1 - f_2$, the beat frequency is therefore related to the difference in carrier concentrations. This can therefore be used to measure the strength of the spin-orbit coupling, termed the Rashba factor α (see Appendix B). An example of how clear beats in Shubnikov-de Haas oscillations manifest in our data can be seen in Figure 8. In our samples, only EP1 shows clear beats indicative of spin-orbit coupling.

3 Project Overview

Next, we review the methods used in this project.

3.1 Heterostructures

The samples used in this project are group III-V heterostructures grown with molecular beam epitaxy at the Naval Research Laboratory. EP1 is a commercially bought sample with a deep quantum well. Test results show that EP1 has excellent semiconducting properties and strong spin-

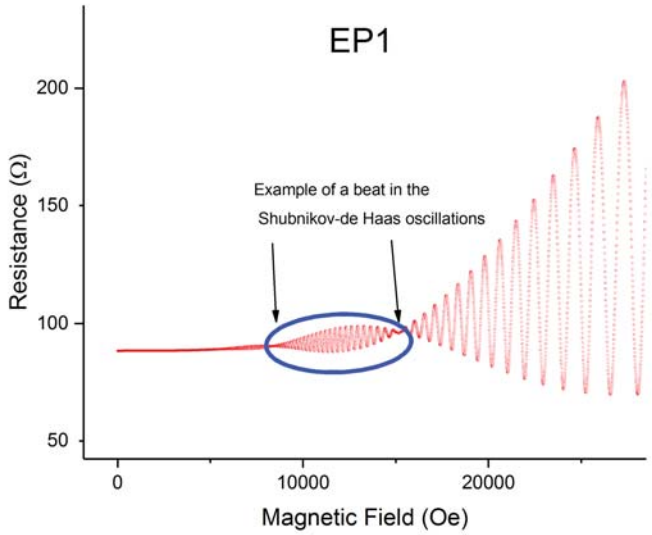

Figure 8: *Shubnikov-de Haas beats measured at USNA. The circled area indicates beats and therefore spin-orbit coupling.*

orbit coupling. It will be used as a reference point to compare the NRL samples. The sample structure can be seen in Figure 10. The channel is $In_{0.53}Ga_{0.47}As$ /InAs/ $In_{0.53}Ga_{0.47}As$ acting as the quantum well, and the $In_{0.52}Al_{0.48}As$ layers on each side of the channel act as the energy barriers to contain the electron wavefunctions. The charge reservoir lies in the doped 7nm $In_{0.52}Al_{0.48}As$ layer, which is separated from the channel by a buffer layer of 6nm. Although EP1 exhibits excellent properties, the channel is deep, 35nm from the surface. At this depth, the signal from the charge carriers is greatly attenuated at the surface electrodes. This limits its usefulness in spintronic applications.

We have studied samples grown by the Naval Research Laboratory including 01L and 24M. Both samples are bottom doped *n*-type heterostructures. In addition to the bottom doped samples, we have also studied a top-doped sample, 13J. These samples have channels much closer to the surface (within 7-10nm from the surface). In both samples, Tellurium was the chosen dopant for the two dimensional electron gas systems.

The samples have been fabricated into Hall bars with geometry as shown in the Figure 9. The picture shows the metallic contacts and the InAs channel with a width of $80\mu m$ and the closest distance between midpoint contacts is $240\mu m$.

Figure 9: *Optical microscope picture of the Hall bar. The gold rectangles are contact pads and the grey area is the channel processed using photolithograph. Leads are blurred due to optical diffraction.*

3.1.1 Sample Structures

(a) EP1 Sample Structure

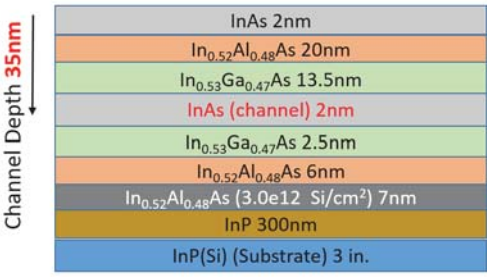

(b) 24M Sample Structure

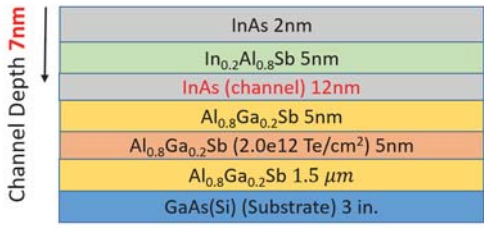

(c) 01L Sample Structure

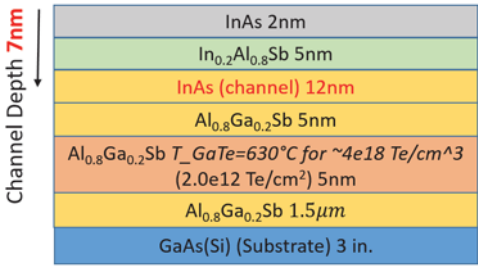

(d) 13J Sample Structure

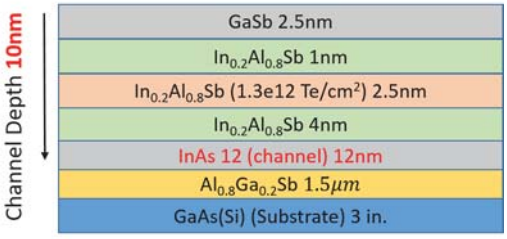

Figure 10: *Sample structures for all of the samples measured. The channel is highlighted in red and depth of each layer are located on the right.*

3.2 Equipment

Figure 11: *PPMS system at USNA*

Available at the US Naval Academy, the main experimental equipment is a **Physical Properties Measurement System (PPMS)** coupled with a helium recirculating system **Evercool II by Quantum Design**. This is a low-temperature and high-magnetic field platform. As it is currently configured, the system can modulate temperature from 1.9 K to 350 K. The magnetic field can be changed from -9 T to +9 T. The PPMS also has a sample rotation option. Using this tool, low-dimensional structures such as our samples can be fully investigated for their anisotropic properties, especially with regard to magnetic field orientation. The PPMS has a light source to analyze samples as they are exposed to light. The light source is a 100W lamp with a color temperature of ≈3200 K. The output from the lamp starts around 350nm. The light intensity can be modulated through a variable voltage supply, allowing us to measure the effect of persistent photoconductivity on our samples. For electrical transport measurements, we use a low-frequency resistance bridge with three channels, which is part of the PPMS system and embedded in the PPMS data acquisition software.

3.3 Measurements

From the clean Shubnikov-de Haas oscillations, we extract the parameters including carrier concentration, effective mass, and quantum scattering time among others. These measurements create a complete portrait of each sample's transport and spin-orbit properties. We also measured the Hall or R_{xy} resistance. The setup for our measurements can be seen in Figure 12. To measure the longitudinal resistance, current flows from I+ to I- and the potential difference is measured along the channel from V+ and V-. The current and voltages are converted to resistance via Ohm's Law. Likewise, for transverse resistance, current is injected the same way but the potential difference is measured across the channel from V+ and V-.

(a) R_{xx} Geometry

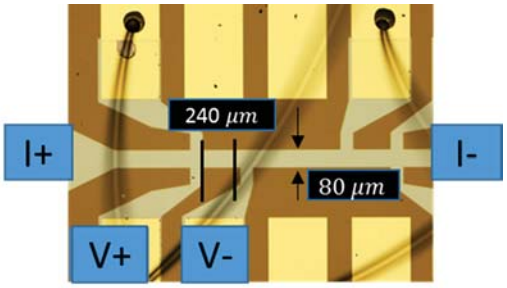

(b) R_{xy} Geometry

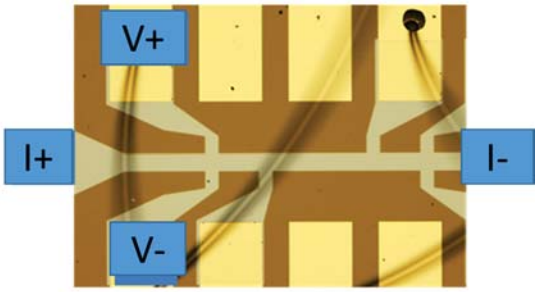

(c) Setup for Optical Illumination

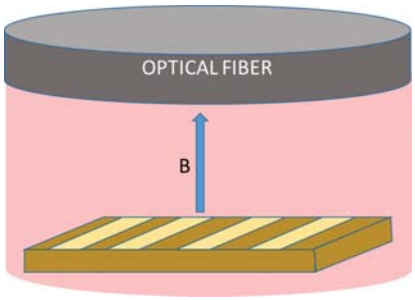

Figure 12: *Experimental setups for longitudinal and transverse resistance as well as the optical illumination.*

4 Process

Analyzing the large amount of data we collected required a great deal of data processing and analysis. The first step of this process was data separation. The data is collected by the PPMS system and divided by sample type. But each data set contains the measurements of the sample under 7 different light conditions and 8 temperatures. Additionally, these data sets contain transition data, which is data taken by the PPMS as it switches to a different temperature or a different wavelength that contains no usable information. So each data set must be analyzed individually and split up by temperature and wavelength. A flowchart illustrating the process can be seen in Figure 13. In total, with four samples and eight temperature conditions and seven light conditions, we have analyzed 224 sets of data.

Examples of the types of data we collected can be seen in the Figure 14. Looking at the graphs, we can see how the various illumination conditions change the oscillation frequency, the beat location (for EP1 only), the zero-field resistance, and the background radiation. The temperature conditions demonstrate the temperature dependence of the oscillations.

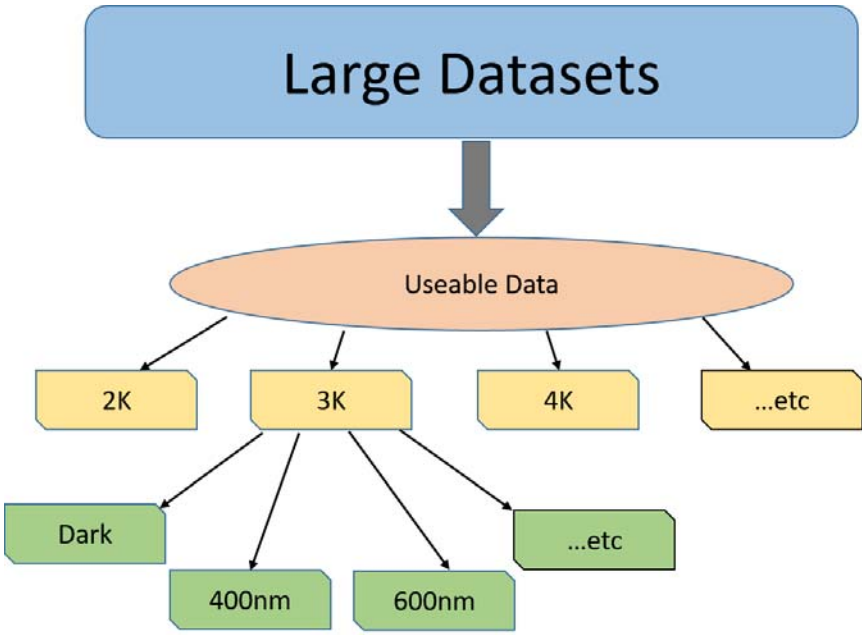

Figure 13: *Flowchart demonstrating the data filtering and separation required before data analysis can occur.*

4.1 Noise Filtering

The next portion involves smoothing out the data set to remove noise. The data taken contains noise at a minute level. To remove the noise but keep the overall trend of the data, we averaged each data point with the five points that proceed it and the five points that follow it. An example of how this changes our signal can be seen in Figure 15. The black data is the original noisy data, while the red data has been averaged to reduce noise. Averaging the data with the surrounding points eliminates false local minima/maxima and adds to the accuracy of our measurements. Furthermore, it has a negligible effect on the amplitude of the oscillations. Thus, this process enables us to eliminate sample noise while maintaining the integrity of our data and the resulting analysis

4.2 Residual Extraction

The process of subtracting the background resistances to extract a clean signal of Shubnikov-de Haas oscillations proved the most difficult. The difficulty was creating a process to extract a nonlinear trend from oscillatory data without introducing a systematic error into the oscillating data. Our initial solution to this was a simple polynomial fit, which fits the data to an n^{th} order polynomial like $C_n x^n + C_{n-1} x^{n-1} + ... + C_1 x + C_0$. However, we found that these fits were extremely dependent on the data break point and the order of the polynomial. Tuning these fits

(a) EP1 Illumination Conditions

(b) 13J Illumination Conditions

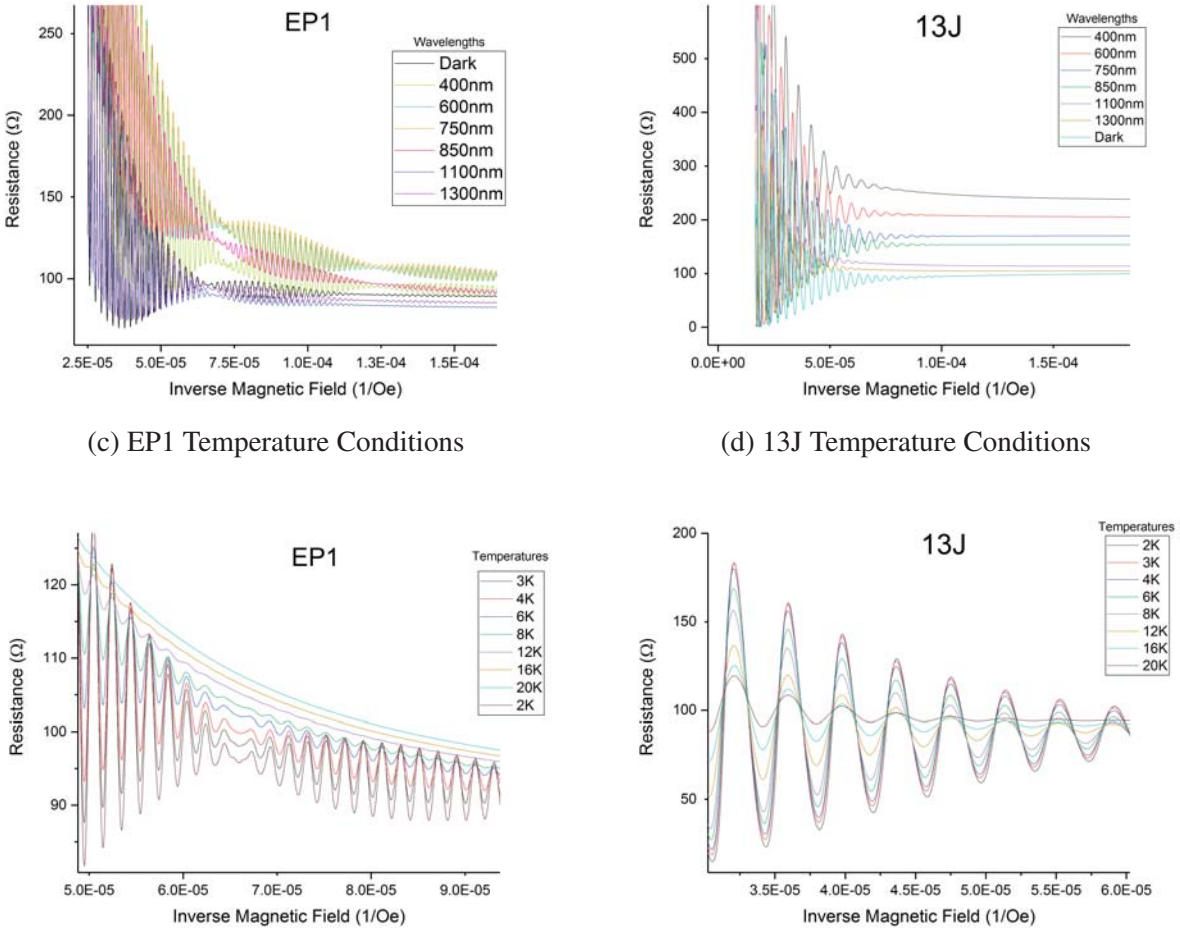

(c) EP1 Temperature Conditions

(d) 13J Temperature Conditions

Figure 14: *The following data was collected from two of our 4 samples under various illumination and temperature conditions.*

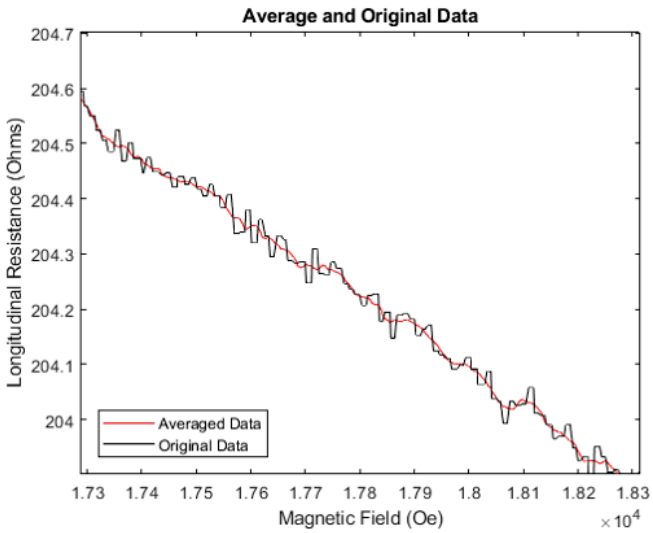

Figure 15: *An example of how averaging the data with the surrounding points can keep the overall data trend while removing noise present in the data.*

took a large amount of time and even after a great deal of effort would not output a good fit. Ultimately, this stemmed from the nature of a least-squares fit. These fits attempt to minimize the residuals in the data, meaning a perfect fit would have a residual of zero. This is exactly what did not want in our data. However, the oscillations in low field were small enough that simple polynomial fits produced good results (see Figure 16).

Instead, in high fields, we turned to a different method of fitting, a cubic smoothing spline. A

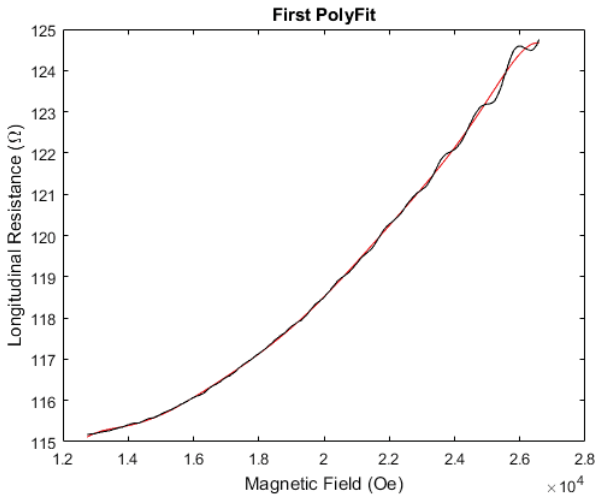

Figure 16: *Low field data (black) is well fitted by a polynomial fit (red).*

spline is a piecewise polynomial like:

$$S(t) = \begin{cases} P_0(t) & t_0 \leq t < t_1 \\ P_1(t) & t_1 \leq t < t_2 \\ \vdots & \vdots \\ P_k(t) & t_k \leq t < t_{k+1} \end{cases}$$

where $P_n(t)$ is a polynomial. In addition, a smoothing spline has a smoothing parameter p that controls the roughness measure of the data. For our data, we found that a smoothing parameter of $p \approx 10^{-12} - 10^{-13}$ works best. A comparison among different polynomial fits to the cubic spline fit in Figure 17 shows that in the high field the spline is a much better fit to the data. Once this fitting was optimized, it enabled a much faster processing of the data with much more accurate results.

However, under a more intense scrutiny, we found that these fits tended to produce a steady state error. Generally, these spline fits would produce a bias towards the higher valued data points. Thus, when examining the absolute value of our residuals, the peaks did not increase monotonically. An example of this error can be seen in Figure 18.

Finally, an accurate method was produced. This method continued to use a simple polynomial fit in the low field region. However, in high field, the fit was produced by finding local maxima and minima. The series of maxima and minima were each fit separately using a cubic smoothing spline with an optimized smoothing parameter. These fits were then averaged to produced a final fit seen in Figure 19. This was the most robust method and ensured that the oscillation peak heights increased monotonically in magnetic field.

5 Parameter Calculation

Once the noise and background resistances were removed, the data that remained was a clean signal of the Shubnikov-de Haas oscillations. From this clean signal, we extracted parameters such as carrier concentration, quantum scattering time, and effective mass. We also sought to measure the spin-orbit coupling strength of our samples. However, only EP1 shows clear beats indicative of spin-orbit coupling. We analyze the reasons behind this fact in the following section.

(a) 4^{th} Order Polynomial

(b) 5^{th} Order Polynomial

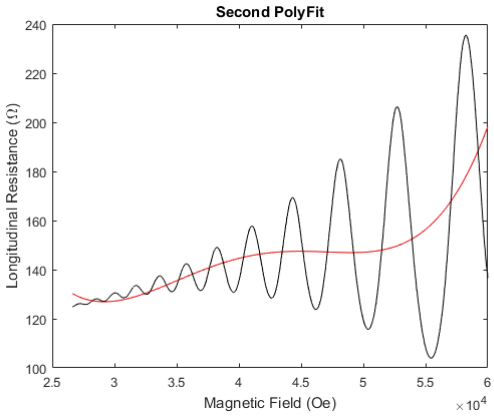

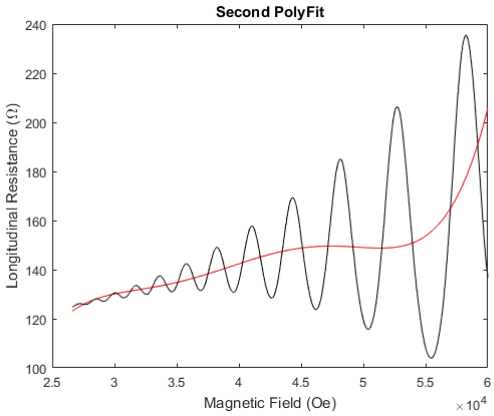

(c) 6^{th} Order Polynomial

(d) Spline Fit

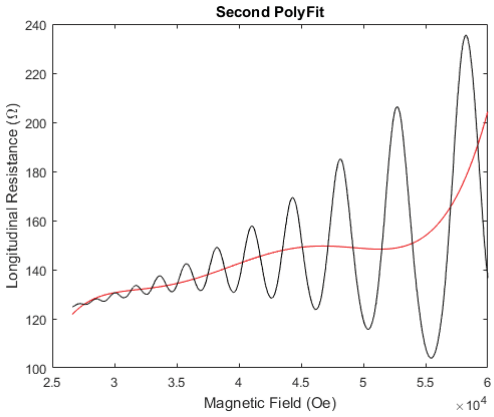

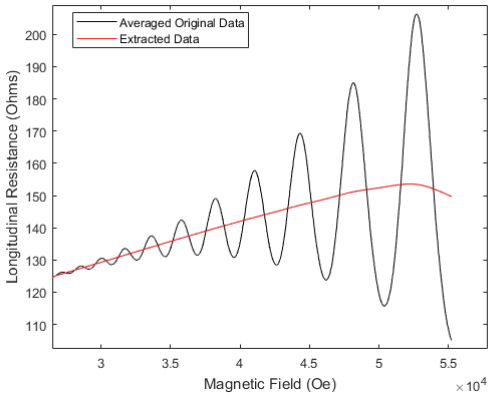

Figure 17: *Above are side-by-side comparisons of the different fits possible with a polynomial fit and a spline fit. The spline fit clearly shows a better fit of the data over the high field range.*

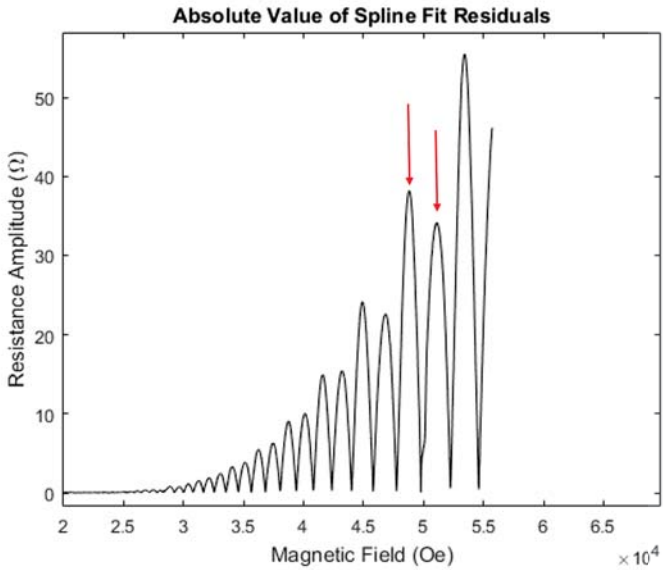

Figure 18: *The spline fit would often produce an error in the signal which was magnified at high oscillation amplitudes. Arrows point to peaks which exhibit obvious issues.*

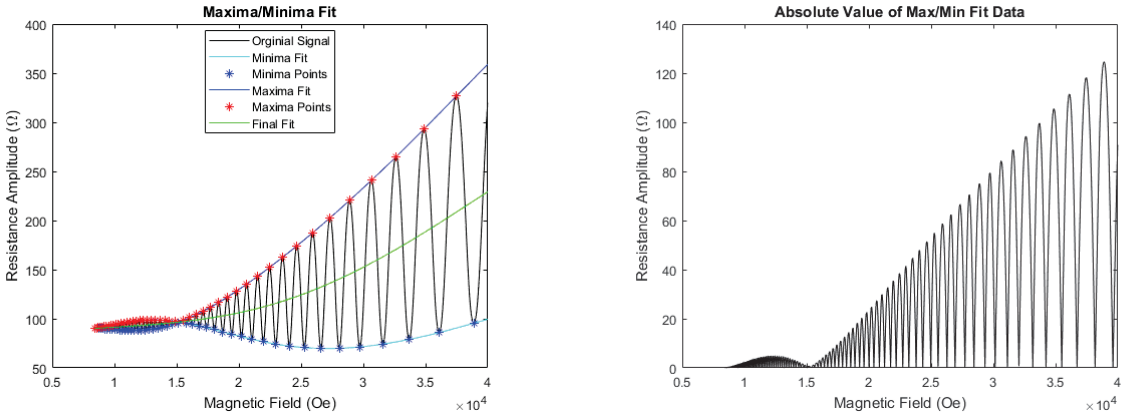

Figure 19: *An example of the high field fitting process using the maxima and minima to produce an averaged fit. The result of this fit provides a clean signal whose peak heights increase in the manner that we expect.*

5.1 Carrier Concentration

The Shubnikov-de Haas oscillations, when analyzed in inverse magnetic field, are periodic. The frequency of the oscillations are dependent on the carrier concentration of the sample like:

$$f = \Delta(\frac{1}{B}) = \frac{hn}{2e}. \tag{4}$$

This equation can then be rearranged to compute the carrier concentration over a full period of 2π.

We look at one period of the oscillations by looking at oscillation maxima. The distance between each maximum in inverse magnetic field is equal to one period. This can then be plugged into the equation for carrier concentration and compute a carrier concentration as a function of magnetic field. While we do not expect a dependency on the magnetic field, this method does allow us to check for consistency in regards to carrier concentration. These measurements were done for all the samples under all light conditions and temperature. The data taken at the lowest temperatures provides the cleanest signal, because it is the least polluted with thermal noise. Figure 20 illustrates carrier concentration data taken from the lowest temperature for all the samples under different light conditions.

The data in Figure 20 shows the effect that light exposure has on the carrier concentration of the samples over a range of magnetic field. Over magnetic field, the carrier concentration is essentially constant. We attribute the variation in the data to the noise in the sample making peak location difficult to determine precisely, especially in low field when the oscillations are well-damped. This is true for all samples, Next, we look at these graphs to create an idea of how the carrier concentration of the samples changes due to light. For EP1, the deep-channel sample, the exposure to the sample of any energy increased its carrier concentration but this effect plateaued in higher energy fields. This is termed positive photoconductivity. For the shallow channel samples including 01L, 24M, and 13J, the samples exhibited both an initial increase and then a decrease in their carrier concentration with the energy of the light. They thus exhibited both positive and negative photoconductivity, which can be seen in Figure 21. This is consistent with published results of samples with similar structures [18]. For 24M, 01L, and 13J, at wavelengths lower than 850nm, the samples exhibited negative photoconductivity. Conversely, at wavelengths of 1100nm and 1300nm, the samples exhibited a large positive photoconductivity. On the other hand, EP1 exhibited only positive photoconductivity and experienced a carrier concentration maximum at around 600nm and 400nm. These lower wavelengths correspond to higher energies. Overall using light exposure, we were able to change the carrier concentration of the samples between roughly 10% and 40% (see Table 1).

(a) Carrier Concentration for EP1

(b) Carrier Concentration for 24M

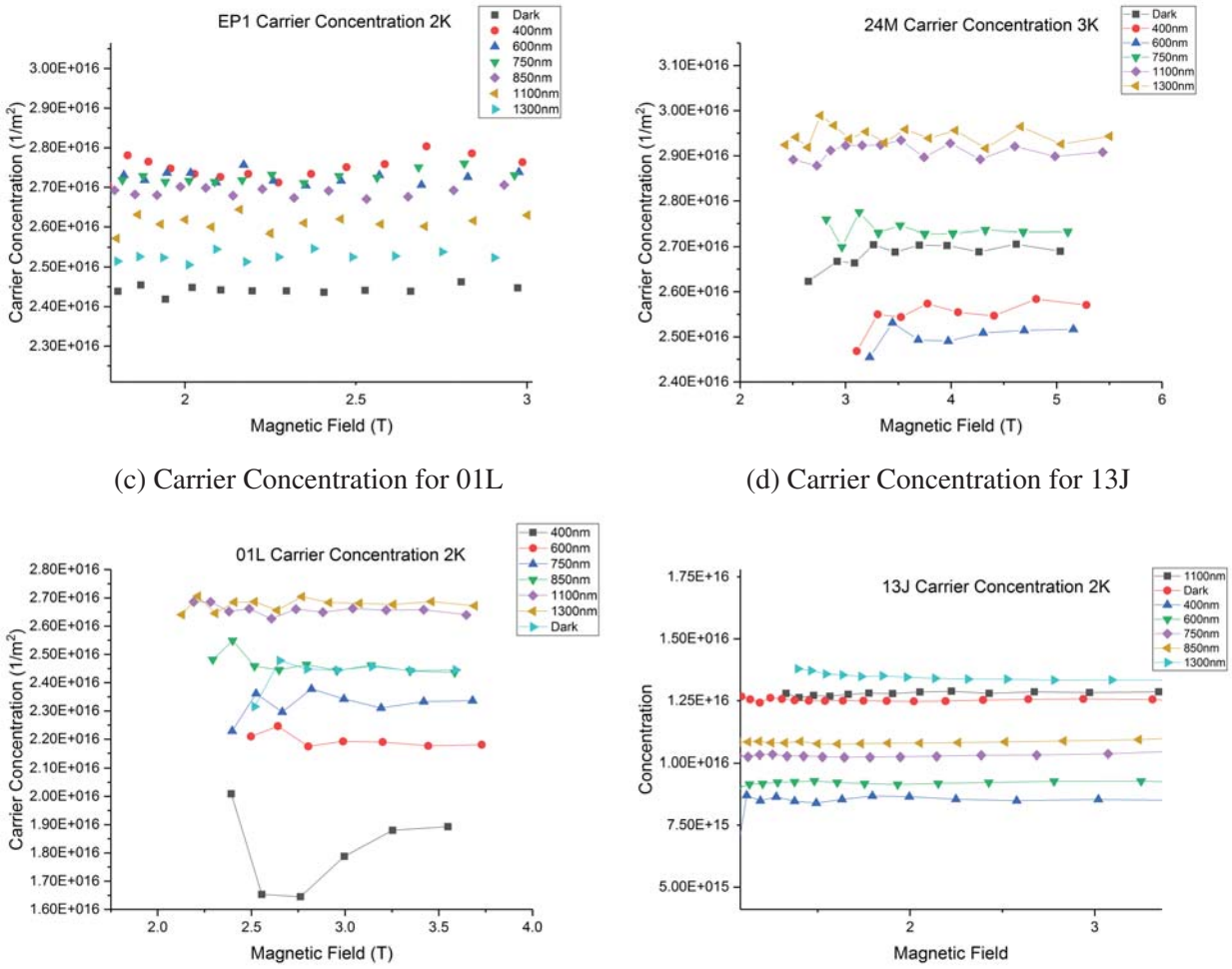

(c) Carrier Concentration for 01L

(d) Carrier Concentration for 13J

Figure 20: *Carrier Concentration for all studied samples as a function of the inverse magnetic field. The different colors represent different light conditions.*

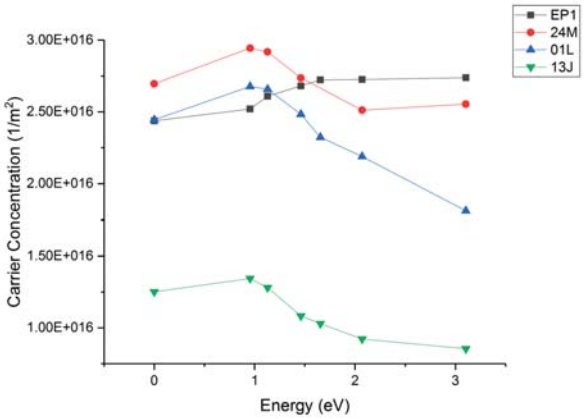

Figure 21: *A comparison among samples of the carrier concentration as a function of the energy of the light exposed. EP1 clearly shows only positive photoconductivity while 24M, 01L, and 13J exhibit negative photoconductivity past a certain threshhold energy.*

Table 1: Reported Carrier Concentration Values

	EP1	24M	13J	011
Dark (n)	2.438e16	2.690e16	1.252e16	2.445e16
Max Δn	3.005e15	4.325e15	4.893e15	8.655e15
Max Variation(%)	12.33	16.07	39.08	35.40

The results create a rough picture of the samples' band structures. Particularly, the results portray what the minimum band-gap between the valence and conduction band might be. Although the reason for the differences has not been determined exactly, we suspect that the composite deep well channel exhibits a different energy band structure than the purely InAs channels in the shallow channel samples.

Most importantly, these results demonstrate our ability to change the carrier concentration of the samples without the fabrication of a gate electrode. Traditionally, gate electrodes were fabricated to change the carrier concentration of the samples through the application of a gate voltage. However, with this technique we have been able to change the carrier concentration by simply shining light on the samples and varying the wavelength. This is a much simpler method to probe the effects of a changing carrier concentration.

5.2 Effective Mass

An electron's effective mass is an important semiconducting property. Effective mass models how an electron in a crystalline lattice responds to an applied electric field. Therefore, an electron in a crystalline lattice under the effect of an applied electric field can be modeled with Newton's Laws

as if it had a mass m^*. Analysis of this parameter requires a more complex analysis method than carrier concentration.

The Shubnikov-de Haas oscillations contain the information necessary to extract effective mass in the temperature dependence of the peak amplitudes. The osciallltion amplitude is governed by:

$$\Delta\rho_{xx}/\rho_{xx}(0) = 2e^{(-\pi/\omega_c\tau_q)}\frac{2\pi^2 k_B T m^*/\hbar eB}{\sinh \pi^2 k_B T m^*/\hbar eB}. \tag{5}$$

The later term contains the temperature dependence which determines the rate at which the amplitude decreases with the temperature increase. Thus, by looking at each peak height as a function of the temperature, we can fit the data to the equation and extract the effective mass. This was done in Matlab using the a nonlinear least squares regression technique. A plot of what a fit looks like for our data is shown in Figure 22. Since each fit is conducted on a peak located at a specific magnetic field, the resulting data shows the effective mass as a function of the applied magnetic field.

Earlier results for the effective mass were skewed due to their dependence on the fitting process. The error introduced in the fitting process skewed the amplitude heights which in turn lead to inaccurate calculations for the effective mass. Using the improved fitting method, we were able to obtain accurate measurements of the effective mass.

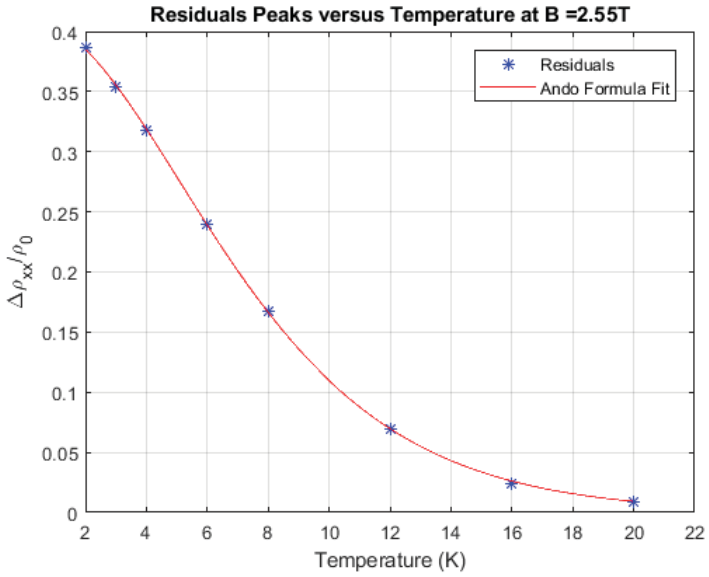

Figure 22: *A temperature dependent fit of the amplitude height for EP1. The red line is the fit we acquired through our model and the blue stars are the data points we extracted from the oscillations.*

The effective mass versus magnetic field data in Figure 23 exhibits a non-linear dependence on the magnetic field. However, the trend is not clear enough to draw conclusions [8]. Additionally,

in the low field, where some of the smaller oscillations die off faster, the fits were performed on a smaller number of datapoints. As a result, the fit is likely to produce less accurate results with less data to guide the fitting process. For all the bottom-doped samples under all the variety of conditions, the effective mass was generally between 5% to 6% of the rest mass of the electron. However, for 13J, the lone top-doped sample, the effective mass lay mainly between 3.5% to 4.5% of the rest mass.

(a) Effective Mass for 01L

(b) Effective Mass for 24M

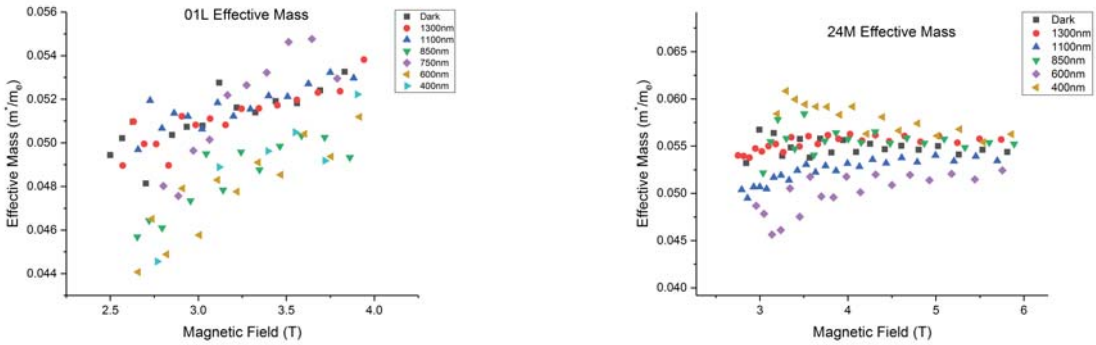

(c) Effective Mass for EP1

(d) Effective Mass for 13J

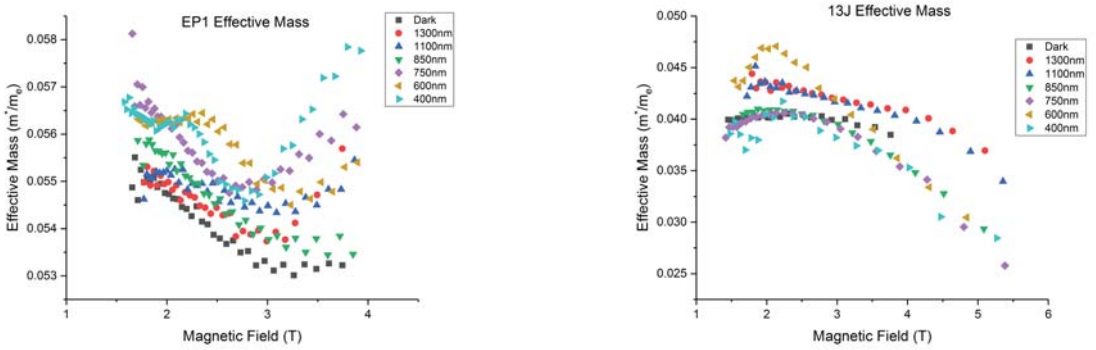

Figure 23: *The Effective Mass for all studied samples as a function of the magnetic field. The different colors represent different light conditions.*

By placing all of this data within the same graph (see Figure 24), we obtain a clearer idea of the amount of variation that exists between samples. Overall, 24M and 01L show very similar responses within the field range measured. The effective mass of EP1 exhibits the least amount of variation as it stays within a narrow band of values. Lastly, 13J exhibits the lowest value for effective mass as well as a decreasing trend with the magnetic field.

The analysis of the effective mass versus light data, as shown in Figure 24, shows no dependence on the energy of the light to which the samples are exposed. This is mainly because our data

(a) Combined effective mass in B-field

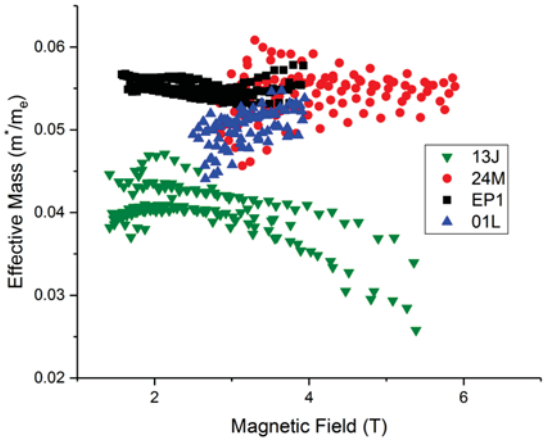

(b) Effective mass versus light energy

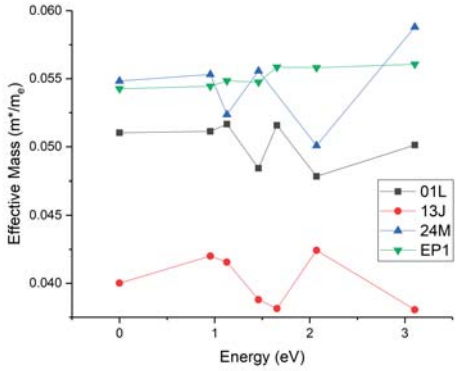

Figure 24: *Combined effective mass data across all the measured samples.*

values are too scattered to see these traits.

Lastly, once the effective mass for each light condition was calculated, the averaged effective mass was compared to the carrier concentration for the corresponding light condition. This allowed us to visually study how the effective mass is affected by the changing number of carriers in the sample. We found that a positive linear relationship exists between the effective mass and the carrier concentration exists among the samples studied. This has been attributed to band non-parabolicity and is consistent with results of other samples of a similar structures. [8]

5.3 Zero-Field Electron Transport Properties

To extract the electron transport properties of the sample including mobility and Drude scattering time, we used zero-field resistance data. Zero-field resistance data is data regarding the resistance of our samples in the absence of a magnetic field. These properties give a more complete portrait of the general carrier properties of the samples absent the effects of a magnetic field.

5.3.1 Mobility

Mobility is a general measure of how easily an electron can flow through the material. Mathematically, it is a measure of the drift velocity response of the electron to an applied magnetic field. However, for this project, we determine the mobility via $\mu = \dfrac{1}{R_s(0)en}$, where $R_s(0)$ is the sheet resistance at zero magnetic field, e is the charge of the electron, and n is the carrier concentration of the sample under the various illumination conditions. The property of mobility best describes the overall transport properties of the sample. We considered only data at a $T = 2K$. From Figure

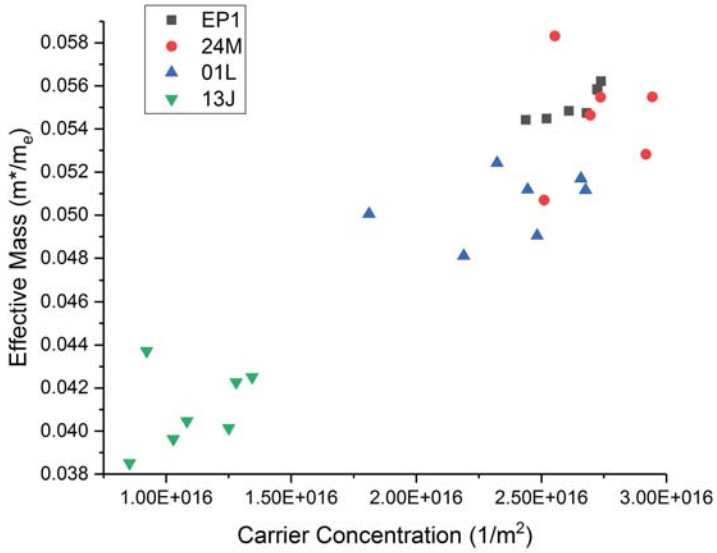

Figure 25: *The mean effective masses of our samples versus the average carrier concentration of the samples at 2 Kelvin.*

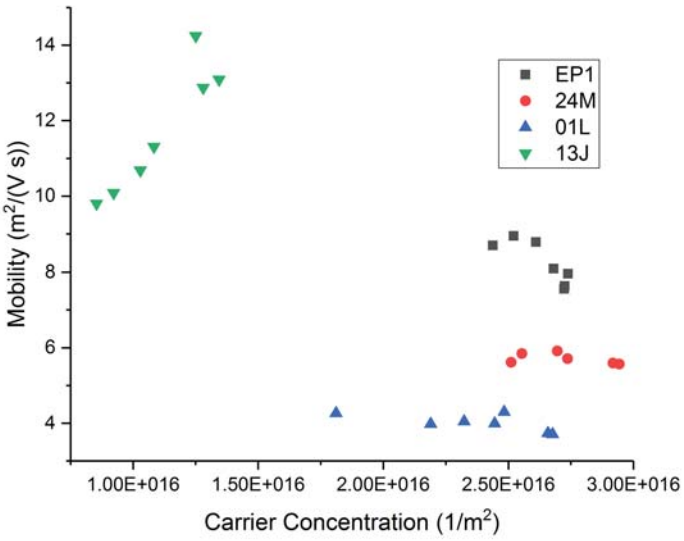

Figure 26: *A graph of the mobility of the samples versus the carrier concentration changed by the illumination conditions.*

27, it is apparent that all our samples display mobilities comparable to EP1. Since EP1 exhibits strong spin-orbit coupling, we conclude that the spin orbit coupling properties are not inhibited by poor mobility.

5.3.2 Drude Relaxation Time

Measurements of mobility can then be used to measure the Drude relaxation time. The Drude relaxation time is a measure of the time between collisions and can be calculated via $\tau_D = \frac{\mu m^*}{e}$. The Drude time is also known as the momentum relaxation time and expresses how scattering events effect the movement of electrons in a sample. The results are plotted in Figure 27. The variation in mobility is directly related to the variation in the Drude time. 01L and 24M have the lowest Drude times, while 13J and EP1 have comparable Drude times.

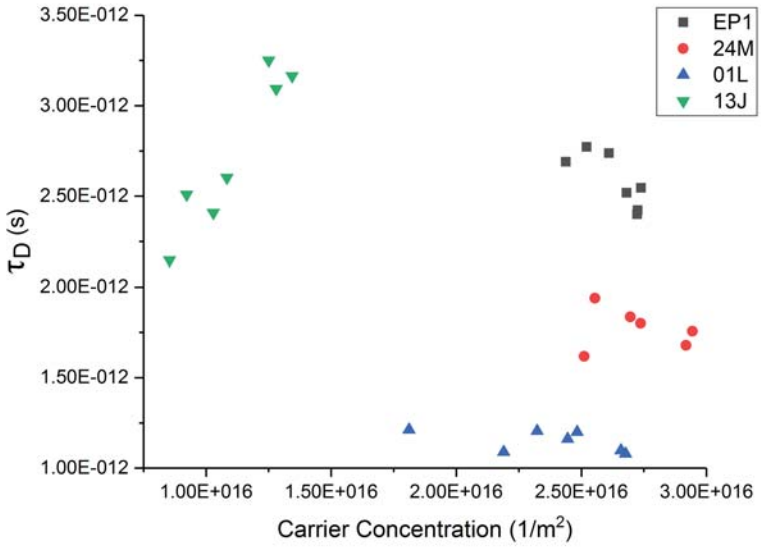

Figure 27: *A graph of the Drude relaxation times of the samples versus the carrier concentration changed by the illumination conditions.*

5.4 Quantum Scattering Time

The last parameter we analyzed in our samples was the quantum scattering time. Quantum scattering time is a measure of how long the carrier stays in a specific state. Additionally, it relates to how broad the Landau level is. Ideally, the Landau level exists at only a particular energy but the Heisenberg Uncertainty Principle states that energy levels have a certain level of broadening. This

broadening is given by $\Gamma = \frac{\hbar}{\tau_q}$.

Quantum scattering time was initially extracted along with effective mass during the temperature dependent fit illustrated in Figure 23. Specifically, the quantum scattering time comes from the exponential decay portion of the Ando formula. The results for quantum scattering time from this initial (albeit inaccurate) fit are shown in Figure 28. The scattering times do exhibit a certain

(a) Scattering Time for 01L

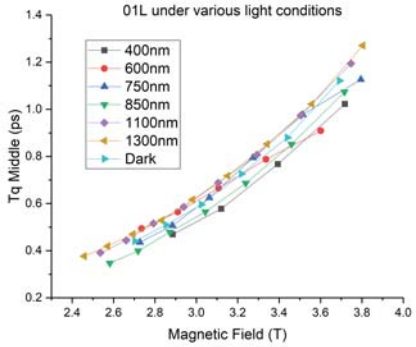

(b) Scattering Time for 24M

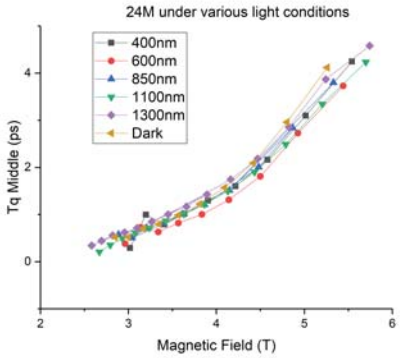

(c) Scattering Time for EP1

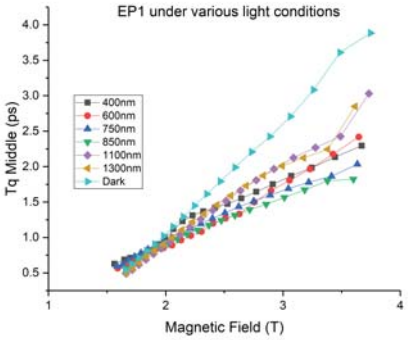

Figure 28: *The quantum scattering times for all studied samples as a function of the magnetic field. The different colors represent different light conditions.*

dependence on the magnetic field. However, further analysis will demonstrate why these results may not represent the true dependence of the scattering time on the magnetic field.

The most important information gained from this fit is that at a given magnetic field the quantum scattering time for EP1 is at least twice as large as the scattering times of 24M and 01L. This is more evident in Figure 30. We explore this further in our paper.

5.4.1 Dingle Plots

Although the quantum scattering times exhibit a certain dependence on the magnetic field in our results, the concept of a Dingle plot points to a limit on the Ando formula ability to fully model our system throughout the entire range of magnetic fields. To look at a Dingle plot, the Ando formula must be rewritten as:

$$\Delta\rho_{xx}/\rho_0 = A\frac{bT}{\sinh(bT)}, \tag{6}$$

where $A = 2\exp\left(-\frac{\pi}{\omega_c\tau_q}\right)$ and $b = 2\pi^2 k_b/\hbar\omega_c$. As a result, b contains only effective mass dependence and the A contains all the quantum scattering dependence. Therefore, plotting the natural logarithm of $\frac{\Delta\rho_{xx}/\rho_0}{bT/\sinh(bT)}$ should yield a plot which is linear in inverse magnetic field. This is shown below:

$$\ln\left(\frac{\Delta\rho_{xx}/\rho_0}{bT/\sinh(bT)}\right) = -\frac{\pi m^*}{e\tau_q}\left(\frac{1}{B}\right) + C. \tag{7}$$

This is equivalent to plotting the natural logarithm of the coefficient A which is found again using a nonlinear least squares fit in Matlab. The graphs for these are depicted in Figure 29.

The Dingle plots shown in Figure 29 display a relatively linear signal for the samples 01L and 24M, but the graph for EP1 displays a clearly non-linear trend. A linear trend for the Dingle plots indicates that the Ando formula is an appropriate model for the range of magnetic field we consider. However, a non-linear trend indicates that the model may not be entirely appropriate over the entire range [19]. An important point to note when analyzing these plots is the range of inverse field the plots cover. Although all plots show data starting at 0.20 $1/T$, 24M and 01L cover data only to around 0.40 $1/T$ while EP1 has data until 0.60 $1/T$. The data for EP1 was a much cleaner signal allowing oscillations to be seen at much lower magnetic fields. Additionally, the non-linear portion of the data for EP1 occurs only after around 0.40 $1/T$. At inverse fields this high, data for 24M and 01L does not exist. This provokes a question over whether the data for 01L and 24M is good or whether the signal prevents us from seeing these non-linearities. Although the data does not provide clear answers, overall, the Dingle plots suggest that the results for quantum scattering time should be taken with a grain of salt.

5.4.2 Quantum Scattering Time Revisited

Because the quantum scattering time cannot be taken from a simple fit of the Ando formula, a more detailed understanding of the Shubnikov-de Haas oscillations is necessary. Although the original Ando formula accounts for single carrier oscillations, it does not account for spin-split carrier populations, and as a result, it is not valid in the range of high field. As discussed earlier, these

(a) Dingle Plot for 01L

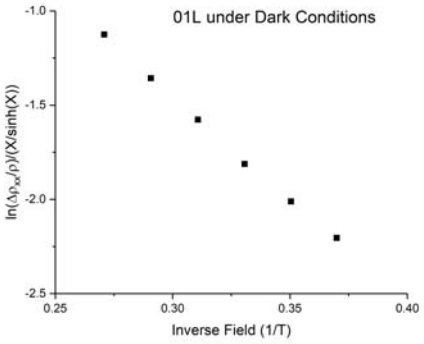

(b) Dingle Plot for 24M

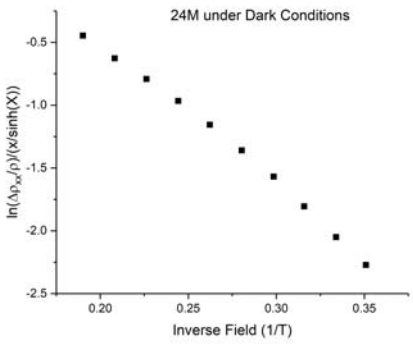

(c) Dingle Plot for EP1

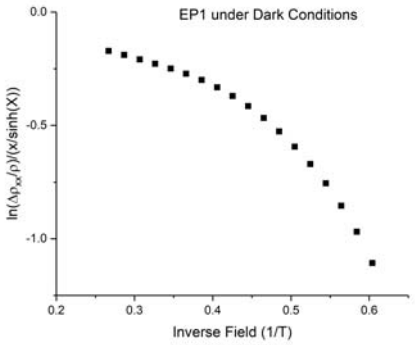

Figure 29: *The Dingle Plots for all three samples under dark conditions. Note that EP1 has data available over a much broader range, giving a more complete picture.*

spin-split populations introduce a beat in the oscillations. This split becomes more pronounced in high field. A more accurate relationship using the Green's function of an electron with spin-orbit interaction in a magnetic field was found by researchers from the Russian Academy of Sciences [20]. Using their work, the relationship of density of carriers to the resistance, and our prior results concerning temperature dependence of the oscillations, we determined the following relationship:

$$\Delta\rho_{xx} = 4\rho_0 \exp\left(\frac{-\pi}{\omega_c\tau_q}\right) \frac{2\pi^2\frac{k_bT}{\hbar\omega_c}}{\sinh\left(2\pi^2\frac{k_bT}{\hbar\omega_c}\right)} \cos\left(\frac{2\pi hn}{2eB}\right) \cos\left(\pi\frac{\Omega_b}{\omega_c}\right). \tag{8}$$

Here the first cosine term accounts for Shubikov-de Haas oscillations and the second cosine term accounts for the spin-splitting (and to a lesser extent in the intermediate field range, the Zeeman effect) which creates the beats. In the latter cosine term, Ω_B is the spin-splitting energy and ω_c is the cyclotron frequency. This analysis can be improved when looking only at points when the cosine terms are equal to 1 and at a single temperature. These terms appear as the peak of a rounded mound in a logarithmic plot of the residuals. To perform an accurate analysis, the temperature dependence term must be divided out of our ρ_{xx} data. From this, the peak data is selected and a we fit a line to this data. Then we can extract the quantum scattering time in the same manner that we calculated it in the Dingle plots. Instead of looking at the coefficient behavior during a temperature dependent fit, this data analyzes solely the exponential decay portion of the Ando formula for resistance data over a range of magnetic field. This allows us to measure the quantum scattering time as a magnetic field fit rather than as a temperature dependent fit. Therefore, this method provides data from a larger range of data points than the Dingle method.

This method, however, requires two separate types of analysis depending on the whether the sample has obvious beats or not. The NRL samples all lack clear beats so we do not have to consider the beat peaks. The same procedure is performed however, once the temperature dependence is eliminated, the maxima points form a clear linear trend which we extract through a fit. Only EP1 shows clear beats and therefore required the first method. The NRL samples did not show clear beats and were fitted using the second method. An example of each fit type can be seen in Figure 30.

Through this fitting process, we confirmed that the deep-channel sample, EP1, has quantum scattering times an order of magnitude higher than those of the shallow well samples. Since the Landau level broadening, given by $\Gamma = \hbar/\tau_q$, is inversely proportional to the quantum scattering time, the Landau levels of the shallow samples are much broader than those of EP1. As a result, if the carrier populations are split by spin-orbit coupling, the Landau levels are also split. However,

(a) Fit with Beats

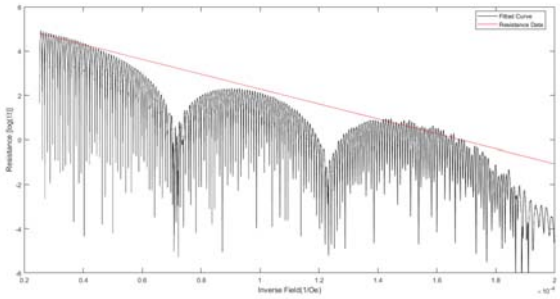

(b) Fit without Beats

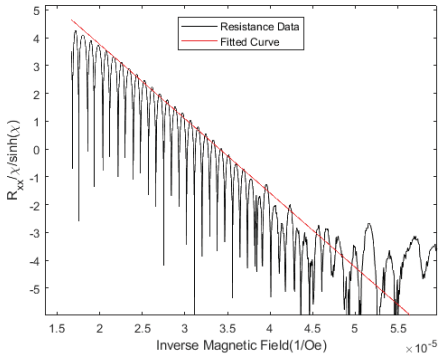

Figure 30: *Example of each type of quantum scattering time fit used for samples with clear beats and without clear beats*

if the Landau level is sufficiently broad, this splitting may be difficult to resolve. Thus, we cannot conclude that spin-orbit coupling is not present in the samples.

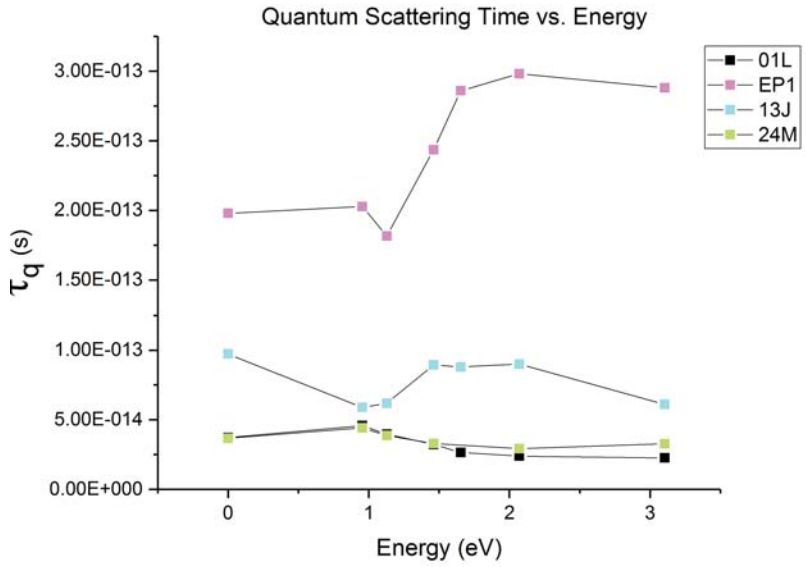

Figure 31: *Quantum scattering times versus energy for all samples under different light conditions.*

5.5 Lande-G and Spin Split Energy

This more detailed look at the Shubikov-de Haas oscillations also enables the calculation of the Lande-g factor as well as the spin-split energy Ω. The second cosine term contains the term Ω_B. This term expresses the spin splitting energy due to both low to intermediate field spin-orbit cou-

Table 2: Reported Values of the Basic Semiconducting Properties

Samples .	n(m^{-2})	$m^*(m^*/m_0)$	τ_D (ps)	$\mu\ (m^2/(Vs)$	τ_q(ps)
EP1	2.44E+16	0.05426	2.68	8.694	0.198
01L	2.45E+16	0.05103	1.16	3.991	0.037
24M	2.70E+16	0.05483	1.84	5.911	0.037
13J	1.25E+16	0.04001	3.24	14.241	0.0973

pling and high field Zeeman effect and can be expanded via:

$$\Omega_B = \sqrt{\Omega^2 + 4\omega_c^2\delta^2} \tag{9}$$

In this equation, Ω is the spin splitting energy and $2\omega_c\delta$ is the energy from Zeeman splitting. Uncoupling these two terms, we can find the spin splitting energy due to spin-orbit coupling. This energy is dependent on the magnetic field at the kth-node point and can be determined through a fit of the following equation:

$$B_k = \frac{2m^*}{\hbar e}\frac{\Omega}{\sqrt{(2k+1)^2 - (g-2)^2}}. \tag{10}$$

To fit the equation to a specific value of Ω and g, we selected the three node points found in EP1 data at a temperature of 2K which corresponded to the specific integers k. From this point, we performed a non-linear least squares fit to ascertain the values of Ω and g. The values of g and Ω we found were consistent with results of similar samples by other researchers [8]. These results combined with the quantum scattering time results mentioned earlier, give strong evidence that the modified relationship above is accurate.

From the spin-splitting Ω, we can extract the Rashba term α. These two terms are related by

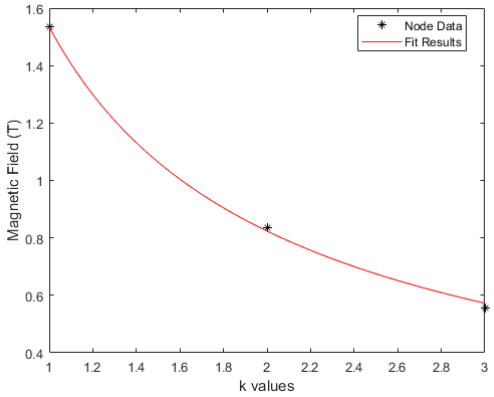

Figure 32: *An example of the fit used to ascertain the value of spin-splitting Ω and the g-factor.*

$\Omega = 2\alpha\sqrt{2\pi n_s}$. The following table contains the values for these quantities calculated through this fitting process.

Table 3: Reported Values of Spin Splitting Properties

Light Condition (nm)	Ω (meV)	α (eV-m)	g-factor
Dark	4.14828	5.30E-12	3.6
1300	4.17451	5.27E-12	3.4
1100	4.16275	5.20E-12	3.31
850	4.05363	4.95E-12	3.3
750	3.99699	4.75E-12	3.12
600	3.97172	4.81E-12	3.29
400	3.84542	4.64E-12	3.25

5.6 Fourier Transform

The Fourier Transform is an additional method for looking at the carrier concentration of the samples. However, this method analyzes the carrier concentration over the entire range of the magnetic field rather than as a function of the magnetic field. This is also the primary method for identifying spin-orbit coupling in our samples. In spin-split samples, there are two separate populations of electrons which create two frequencies in the Shubnikov-de Haas oscillations. In clear signals, this manifests itself as a beat. However, when no clear beats exist, the Fourier Transform provides a more robust way to separate the carrier concentrations.

The Fourier Transform used in this project is modified to provide increase resolution and clarity of output signal. This is done partly through padding the sample data with zeros, which increases the spectral resolution of the discrete Fourier Transform [21]. Additionally, we apply a smooth windowing function to our data set to minimize the contribution the hard bourdaries have on the output signal [8]. The result is a clean output signal.

The Fourier Transform results confirm that 24M, 01L, and 13J do not show evidence of spin-split carrier populations while EP1 shows strong evidence of spin splitting. This is in line with what is visible in the raw Shubnikov-de Haas oscillations.

Since EP1 does exhibit clear beats evident in the spin-split peaks of the carrier concentrations, we can use the Fourier transforms of EP1 to calculate the spin-split energies as well as the Rashba factors through an additional method. We compare these methods in Figure 35. Both methods give values reasonably close but the nodal analysis data has less noise in it. The noise in the Fourier data is a product of the discrete nature of the Fourier analysis, which makes precise peak location difficult to determine exactly.

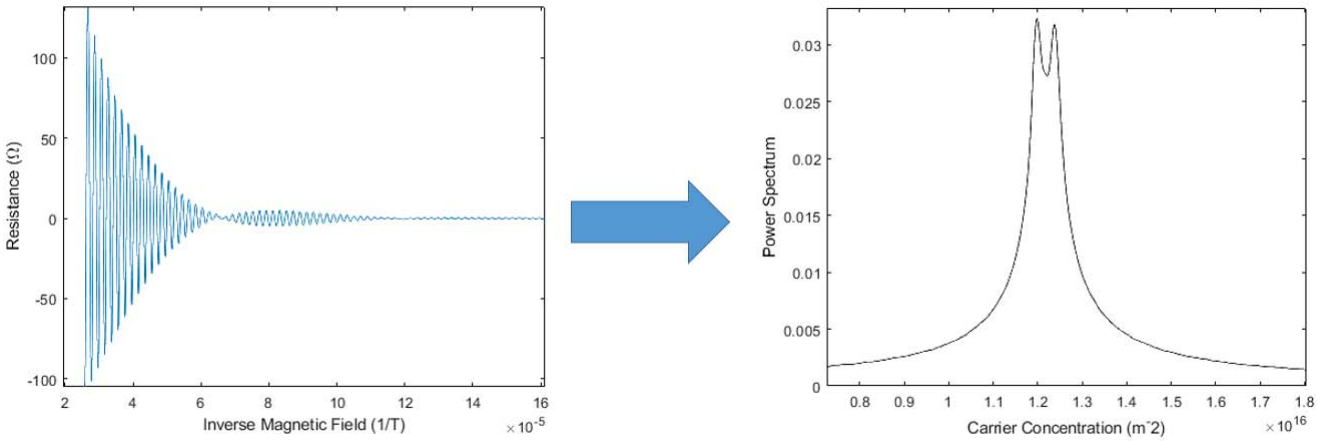

Figure 33: *On the right, the residual input signal and on the left the ouput signal. The beats on the left indicate spin orbit coupling while the split peaks on the right inidicate the same.*

(a) 01L at T=2K

(b) 24M at T=3K

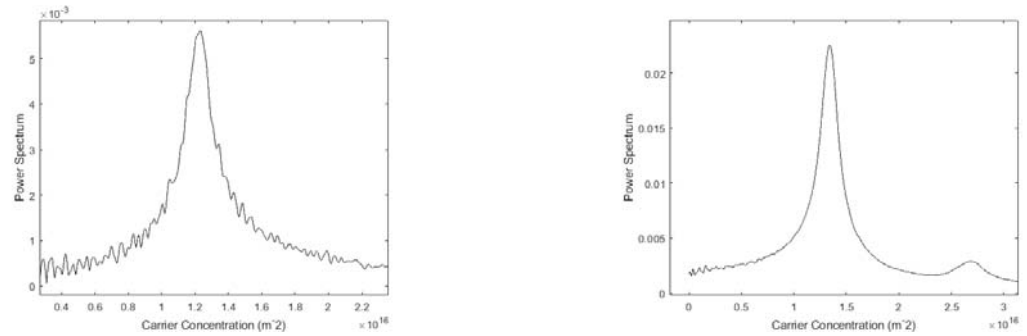

(c) EP1 at T=2K

(d) 13J at T=2K

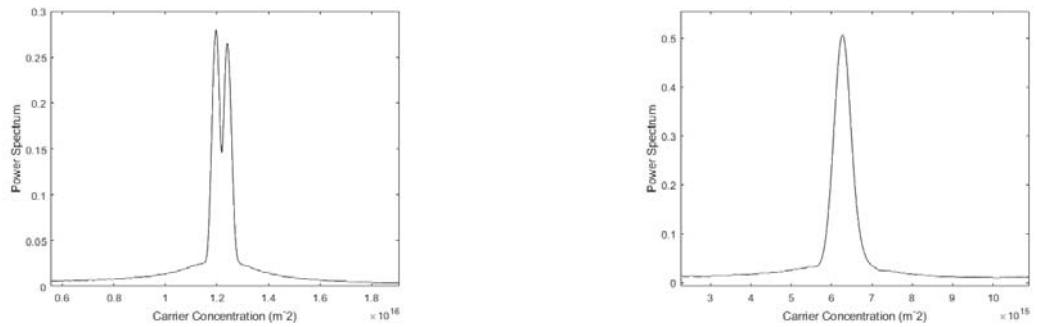

Figure 34: *The Fast Fourier Transforms (FFT) for all samples under dark conditions. Only EP1 has split peaks indicative of strong spin-orbit coupling.*

(a) Spin-Split Energy Ω Comparison

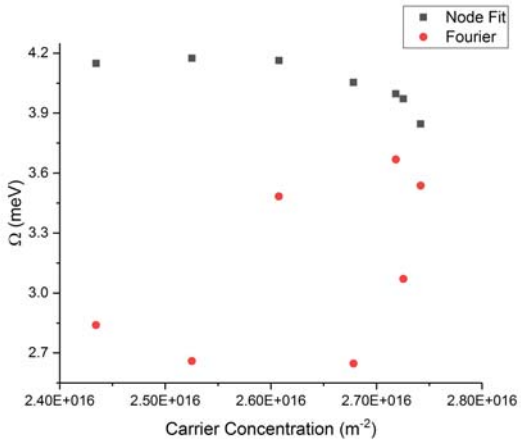

(b) Rashba Factor α Comparison

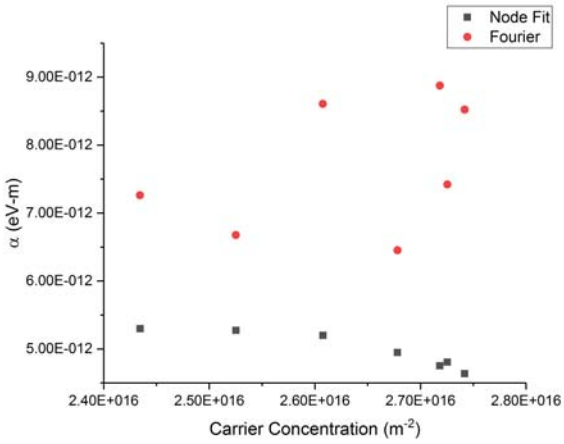

Figure 35: *Comparisons of the Rashba factors and Spin-Splitting energies EP1 calculated via the Node Fit (black) and the Fourier Transform (red).*

6 Conclusion

We found that the persistent application of light can effectively change the carrier concentration without the fabrication of a gate electrode. Additionally, the effective mass exhibited a non-trivial dependence on the magnetic field, the origin of which needs to be further clarified. Nevertheless, our samples manifested a proportional relationship between effective mass and carrier concentration.

Despite the excellent semiconducting properties from all the NRL samples, none of them exhibited clean beats indicative of strong spin-orbit coupling. The clear differences between the samples are the values of the quantum scattering time. The deep-well commercial sample had a scattering time an order of magnitude larger than the shallow-well NRL samples. We conclude that smaller scattering times from the NRL samples smear out the Landau level making the presence of spin-orbit coupling difficult to resolve. This may prevent spin currents from staying coherent in a Spin FET and may make them unfeasible for use in this application. Since all these samples are located within 7-10nm of the surface, we conclude that the surface defects of the samples impedes the direct observation of spin-orbit coupling. We suspect the surface defects introduce low-angle scattering events into the channel which is known to suppress the value of the quantum scattering times [22].

References

[1] D. Bercioux and P. Lucignano, "Quantum transport in rashba spin–orbit materials: a review," *Reports on Progress in Physics*, vol. 78, no. 10, p. 106001, 2015. [Online]. Available: http://stacks.iop.org/0034-4885/78/i=10/a=106001

[2] S. Datta and B. Das, "Electronic analog of the electro-optic modulator," *Applied Physics Letters*, vol. 56, no. 7, pp. 665–667, 1990. [Online]. Available: https://doi.org/10.1063/1.102730

[3] H. C. Koo, J. H. Kwon, J. Eom, J. Chang, S. H. Han, and M. Johnson, "Control of spin precession in a spin-injected field effect transistor," *Science*, vol. 325, no. 5947, pp. 1515–1518, 2009. [Online]. Available: http://science.sciencemag.org/content/325/5947/1515

[4] J. Nitta, T. Akazaki, H. Takayanagi, and T. Enoki, "Gate control of spin-orbit interaction in inverted $In_{0.53}Ga_{0.47}As/In_{0.52}Al_{0.48}As$ heterostructure," *Phys. Rev. Lett.*, vol. 78, pp. 1335–1338, Feb 1997. [Online]. Available: https://link.aps.org/doi/10.1103/PhysRevLett.78.1335

[5] J. Balakrishnan, "Spin transport studies in graphene," Ph.D. dissertation, •, 2013.

[6] S. Gasiorowicz, *Quantum Physics*. John Wiley & Sons, 2003.

[7] A. Avsar, "Charge and spin transport in graphene-based devices," Ph.D. dissertation, •, 2014.

[8] F. Nichele, "Transport experiments in two-dimensional systems with strong spin-orbit interaction," Ph.D. dissertation, ETH Zurich, 2014.

[9] M. Chapman and C. S. de Melo, "Atoms playing dress-up," *Nature*, 2011.

[10] S. Sasa, K. Anjiki, T. Yamaguchi, and M. Inoue, "Electron transport in a large spin-splitting 2deg in $InAs/AlGaSb$ heterostructures," *Physica B: Condensed Matter*, vol. 272, no. 1, pp. 149 – 152, 1999. [Online]. Available: http://www.sciencedirect.com/science/article/pii/S0921452699003786

[11] V. N. Zverev, M. Muhammad, S. Rahman, P. Debray, M. Saglam, J. Sigmund, and H. L. Hartnagel, "Magnetotransport properties of two-dimensional electron gas in $AlSbInAs$ quantum well structures designed for device applications," *Journal of Applied Physics*, vol. 96, no. 11, pp. 6353–6356, 2004. [Online]. Available: https://doi.org/10.1063/1.1792385

[12] Diagram courtesy of Mark Johnson, NSI New Start.

[13] C. Kittel, *Introduction to Solid State Physics*, 8th ed. Wiley, 2005.

[14] Adapted from http://energyeducation.ca/encyclopedia/Band_gap.

[15] Adapted from https://www.redarc.com.au/how-do-solar-panels-work.

[16] J. Schurr, F. Ahlers, and B. P. Kibble, "The ac quantum hall resistance as an electrical impedance standard and its role in the si," *Measurement Science and Technology*, vol. 23, no. 12, p. 124009, 2012. [Online]. Available: http://stacks.iop.org/0957-0233/23/i=12/a=124009

[17] K. S. Cho, T.-Y. Huang, C.-P. Huang, Y.-H. Chiu, C.-T. Liang, Y. F. Chen, and I. Lo, "Exchange-enhanced g-factors in an $Al_{0.25}Ga_{0.75}NGaN$ two-dimensional electron system," *Journal of Applied Physics*, vol. 96, no. 12, pp. 7370–7373, 2004. [Online]. Available: https://doi.org/10.1063/1.1815390

[18] F. Wang, W. E. Zhang, C. H. Yang, M. J. Yang, and B. R. Bennett, "Observation of electrically resettable negative persistent photoconductivity in $InAs/AlSb$ single quantum wells," *Applied Physics Letters*, vol. 69, no. 10, pp. 1417–1419, 1996. [Online]. Available: https://doi.org/10.1063/1.117600

[19] S. Brosig, "Transport measurements on inas/alsb quantum wells," Ph.D. dissertation, ETH Zurich, 2000.

[20] S. G. Novokshonov and A. G. Groshev, "Diffusive magnetotransport in a two-dimensional electron gas in the presence of rashba spin-orbit interaction," *Phys. Rev. B*, vol. 74, p. 245333, Dec 2006. [Online]. Available: https://link.aps.org/doi/10.1103/PhysRevB.74.245333

[21] D. Rowell, "2.161 signal processing: Continuous and discrete," Massachusetts Institute of Technology, MIT OpenCourseWare, Tech. Rep., 2018.

[22] P. T. Coleridge, "Small-angle scattering in two-dimensional electron gases," *Phys. Rev. B*, vol. 44, pp. 3793–3801, Aug 1991. [Online]. Available: https://link.aps.org/doi/10.1103/PhysRevB.44.3793

[23] N. Zettili, *Quantum Mechanic: Concepts and Applications*. Wiley, 2009.

[24] *Heterostructures and Quantum Devices*. Academy Press, 1994, ch. Heterostructures and Quantum Well Physics.

A Spin and Spin-Orbit Coupling

This project is heavily reliant on the electron's spin in relation to spin orbit coupling. However, in the simple model of electrons orbiting the nucleus, electrons also have orbit angular momentum due to their movement around the nucleus. The angular momentum of a particle with respect to a defined origin, in this case the nucleus, is given by:

$$\vec{L} = \vec{r} \times \vec{p}, \tag{11}$$

where $\vec{r}$ is the position vector and $\vec{p}$ is the momentum vector. From classical electrodynamics, we know that a charged particle with angular momentum creates a magnetic dipole given by:

$$\vec{\mu}_L = \frac{q}{2mc}\vec{L}. \tag{12}$$

The spin also creates an intrinsic magnetic dipole moment in the electron in an analogous fashion. This moment is given by:

$$\vec{\mu}_S = -g\frac{e}{2mc}\vec{S}, \tag{13}$$

where g is the g-factor. In the electron's rest frame, the electron sees the proton orbiting it with a velocity equal to $\vec{v} = -\vec{p}/m$. This creates a magnetic field given by

$$\vec{B} = -\frac{1}{c}(\vec{v} \times \vec{E}) = \frac{1}{m}(\vec{E} \times \vec{p}). \tag{14}$$

The magnetic moment of the electron, acting like a miniature magnet, couples with the magnetic field created by the orbital motion of the electron. This coupling produces an energy term in the electron's Hamiltonian like

$$H_{SO} = -\vec{\mu}_S \bullet \vec{B} = -\frac{ge}{2m^*c^2}\vec{S} \bullet (\frac{Ze\vec{r}}{r^3} \times \vec{p}) = \frac{gZe^2}{4m^{*2}c^2}\frac{1}{r^3}\vec{S} \bullet \vec{L} \tag{15}$$

where the extra factor of $\frac{1}{2}$ is a product of relativity [23]. In solids, the magnetic field which the electron couples with is created due when the electron moves through the lattice and experience field asymmetries. In the crystal lattice, electric field asymmetries exist because of impurities, confinement, boundaries, and external electric fields in the crystal lattice (extrinsic term) and asymmetries that result from the band structure of the lattice (intrinsic term). The intrinsic field asymmetries arise due to two separate mechanisms bulk inversion asymmetry and structure inversion asymmetry. Bulk inversion asymmetry produces the Dresselhaus term. Structure inversion

asymmetry produces the Rashba term which has a linear dependence on the crystal momentum $\vec{k}$ [10] [11]. Spin-orbit coupling in quantum well structures stems primarily from the structure inversion asymmetry and manifests itself in the form of beats in what are called Shubnikov-de Haas (SdH) oscillations.

B Spin Splitting Energy

In the absence of a magnetic field the energy is quadratically related to the electron wavevector. However, the presence of spin induces another term to appear in the energy dependence [13] [16].

$$E_{\pm} = \frac{\hbar^2 k^2}{2m} \pm \alpha|k|, \tag{16}$$

where k is the electrons wavevector, α is the Rashba term, and the energy is in relation to the energy subband. The spin splitting difference between the spin-split populations of electrons is then $\Delta_S = 2\alpha k$. In 2D electron systems, α can be indirectly detected from measurements of the SdH oscillations. In a magnetic field B applied perpendicularly to the plane of the well, the longitudinal resistivity R_{xx} shows oscillations that are evenly spaced in $1/B$. The spin-orbit coupling lifts the electron energy degeneracy and splits electrons with spin-up, with a carrier concentration of n_+, and electrons with spin-down, with a carrier concentration of n_-. The two populations generate SdH oscillations with different frequencies in $1/B$.This spin splitting energy is further related to the carrier concentrations of the spin split populations via

$$\Omega = \frac{2\pi\hbar^2(n_+ - n_-)}{m^*} = 2\alpha\sqrt{2\pi n_S}, \tag{17}$$

where $n_S = n_+ + n_-$ and is the total sheet carrier concentration. These carrier concentrations can be extracted from the beats within the Shubnikov-de Haas oscillations. The spacing between the beats is related by

$$\Delta\frac{1}{B_{Beat}} = \frac{e}{2\pi\hbar}(\frac{1}{n_+ - n_-}). \tag{18}$$

Thus, the observed beats within Shubnikov-de Haas oscillations provide a means to extract these parameters.

C Glossary of Terms

Carrier Concentration- A measure of the charge carriers per unit volume.

Doping- The term used for when impurities are introduced into the crystal with a number of valence electrons which leaves either and excess free electron (n-type or a hole where an electron wants to exist (p-type). This affects the energy structure of the crystal.

Fermi Energy- The highest allowed energy for an electron in an electron gas model.

Fermi Velocity- The velocity between collisions of electrons estimated from the electron gas model.

G-factor- A fundamental measurement that relates the strength of the magnetic moment of a particle, in our case an electron, to its spin.

Heterostructures- A chemical structure whose composition changes as a function of position. Heterostructures are commonly thought of in terms of stacks of materials. [24]

Interger Quantum Hall Effect- The staircase-like dependence that the transverse resistance exhibits as a function of the magnetic field. These are due to the spliting of the Landau levels.

Mobility- A measure of how easily the electron moves through the material.

Rashba α- The parameter which characterizes the strength of the spin-orbit coupling. It is related to the difference in carrier populations for spin-split electrons.

Shallow Wells- The devices we use have shallow wells. The term shallow comes from the position of the channel that the electrons flow through relative to the top of the stack. The term well comes from the electrons being contained within the channel by a well of energy.

Shubnikov-de Haas oscillations (SdH)- Oscillations in the longitudinal resistance as a function of the magnetic field. These are due to the splitting of the Landau levels. **Spin**- The intrinsic angular momentum of the electron, which creates an inherent magnetic dipole μ.

Spin-Orbit Coupling- A relativistic effect where the spin magnetic moment of the electron acts as a mini bar magnet and couples with an effective magnetic field.

Zeeman Effect- The energy split among electrons in the presence of a strong external magnetic field. It is related to the strength of the field and the g-factor.

List of Figures

List of Tables